OPTOELECTRONIC TRANSPORT AND ANTIBACTERIAL PROPERTIES DRIVEN BY SURFACE DEFECTS IN MICRO- AND NANOSCALE OXIDES OF ZINC AND GALLIUM.

by
John Hunter Brannon

Bachelor of Science, 2023
Texas Christian University
Fort Worth, Texas

A Thesis
Submitted to the Faculty of
College of Science and Engineering
Texas Christian University
in partial fulfillment of the requirements for the degree of

Master of Science

November
2025

APPROVAL

OPTOELECTRONIC TRANSPORT AND ANTIBACTERIAL PROPERTIES DRIVEN BY SURFACE DEFECTS IN MICRO- AND NANOSCALE OXIDES OF ZINC AND GALLIUM.

by

John Hunter Brannon

Dissertation approved:

Major Professor

For the College

The page after the title page is intentionally left blank, or it may contain the copyright statement shown below. In either case it is not numbered nor counted.

ACKNOWLEDGEMENTS

I would like to thank my family—especially my mom—for maintaining a close and meaningful connection with me throughout my education and my life in general. I couldn't be luckier to have such wonderful grandparents, always curious about my health and life ambitions. I am deeply grateful to my three brothers and two sisters for continually reaching out to stay in touch with me and ensuring I remain a part of their lives. I would not be the person I am today without these profoundly influential individuals, whose guidance and values have shaped my morals and decisions throughout my life.

I would also like to thank my undergraduate and graduate teachers at Texas Christian University, who helped shape me into the academic I have become. In particular, I want to thank my undergraduate advisor, **Dr. Naumov**, for introducing me to research and for his guidance throughout much of my coursework. My greatest appreciation goes to my graduate advisor, **Dr. Strzhemechny**, whose mentorship continually sharpens my intellect in a challenging yet supportive environment. I would not be the scientist I am today without his generosity in sharing his time to discuss and review topics of interest with me time and again.

I would also like to thank **Dr. Wiglusz and his team** and **Dr. Danchuk** for providing such meaningful experiences in **Wrocław, Poland**, and **Brno, Czechia**, respectively. Their hospitality, care, and insightful advice broadened my perspective and left a lasting impact on both my personal and professional growth.

Finally, I would like to thank my fellow graduate students in the department and the previous Strzhemechny lab graduates **Dr. Dustin Johnson** and **Dr. John Reeks** for fostering a supportive and collaborative environment. It has been a privilege to share this journey with people who understand our common goals and strive to help one another succeed.

TABLE OF CONTENTS

LIST OF FIGURES

INTRODUCTION

Zinc Oxide and β-Gallium Oxide: Overview

Metal oxides are binary compounds composed of metal cations and oxygen anions. They play an important role across a wide range of fields, including electronics and sensing technologies, energy production and conversion, environmental remediation, construction, photovoltaics, food and agriculture, as well as biomedicine and pharmaceuticals [1-2]. Metal oxides exhibit high biological and chemical stability, ease of synthesis, and strong sensitivity for detecting both oxidizing and reducing species [3]. The electrical, optical, and catalytic properties of metal oxides are strongly influenced by the type of metal cation, its oxidation state, coordination geometry, and the bonding between the metal and oxygen atoms. Variations in these factors determine key structural and electronic parameters such as lattice symmetry, band gap, and charge transport mechanisms [4-5].

As the size of these materials decreases, their optical, structural, and electrical properties undergo significant changes. Nano- and microscale materials exhibit distinct functionalities compared to their bulk counterparts due to their large surface area-to-volume ratio. This increased ratio enhances surface-related interactions, leading to greater chemical reactivity [1, 6]. Nanotechnology advancements have expanded applications of metal oxides across numerous fields, including electronics, aerospace, medicine, smart materials, pharmaceuticals, photography, and energy technologies [1,3].

Zinc oxide (ZnO) is an extensively used wide band gap semiconductor. It is a promising candidate for diverse applications in electronics, pharmaceuticals, sensors, and photovoltaics [7]. ZnO has a direct band gap of 3.37 eV at room temperature and a large exciton binding energy of 60 meV [8]. As seen in Figure 1, it crystallizes in an anisotropic hexagonal wurtzite structure,

exhibiting primarily ionic bonding characteristics with partial covalent behavior [9-10]. ZnO has two polar surfaces: (0001)-Zn and $(000\bar{1})$-O. It also has two non-polar surfaces: $(10\bar{1}0)$ and $(11\bar{2}0)$ [11]. Due to its anisotropic structure, there is a macroscopic dipole along the *c*-axis of the crystal lattice. This phenomenon influences surface stability, defect formation, and growth morphology, affecting the material's electronic and optical properties. In addition to its advantageous optoelectronic properties, ZnO is chemically stable and biocompatible, broadening its potential areas of use. Its natural abundance and low-cost synthesis make it sustainable and suitable for mass production [1,6-7].

In micro- and nanoscale ZnO, the increased abundance of surface defects and altered surface chemistry can strongly influence properties of this material [13]. Furthermore, concentrations of surface defects are strongly influenced by the polar and non-polar nature of the

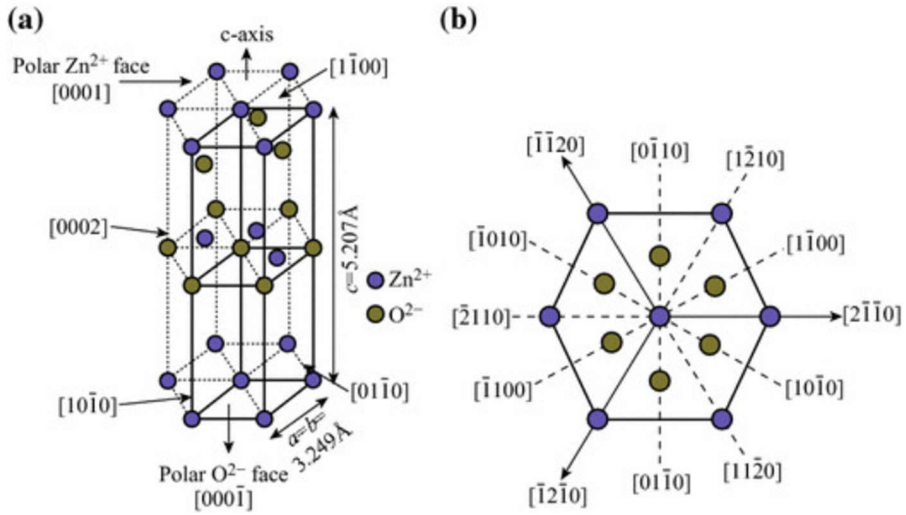

Figure 1: (a) Crystal structure of ZnO exhibiting the hexagonal wurtzite lattice, highlighting the primitive cell configuration and identification of the polar (0001) *and* $(000\bar{1})$ *faces. (b) Top view along the c-axis illustrating the non-polar* $(10\bar{1}0)$ *and* $(11\bar{2}0)$ *surfaces [12].*

surface [14-15]. In nano- and microparticles, the effects of surface defect traps and surface-surface interactions become significantly more pronounced due to the high surface-to-volume ratio [14]. This makes ZnO potent as an antibacterial material [6,16], ***yet the fundamental mechanisms***

responsible for its antimicrobial activity remain unresolved and continue to be actively debated within the field [6, 14, 16-23].

Gallium oxide exists in five known polymorphs: α-, β-, γ-, δ-, and ε. Among these, the α and β phases are the most common. β-Ga_2O_3 is the thermodynamically stable phase under standard conditions, whereas the other polymorphs can transform into this structure under suitable temperature and pressure conditions [25-26]. β-Ga_2O_3 is a wide-bandgap semiconductor that has recently attracted significant attention as an emerging material for next-generation high power electronic devices. It possesses an indirect bandgap of approximately 4.84 eV and a direct bandgap of 4.87 eV. The small energy difference between these two gaps, combined with weak indirect optical transitions, makes β-Ga_2O_3 effectively behave as a direct bandgap semiconductor [24]. Structurally, β-Ga_2O_3 crystallizes in a monoclinic lattice and contains two inequivalent Ga

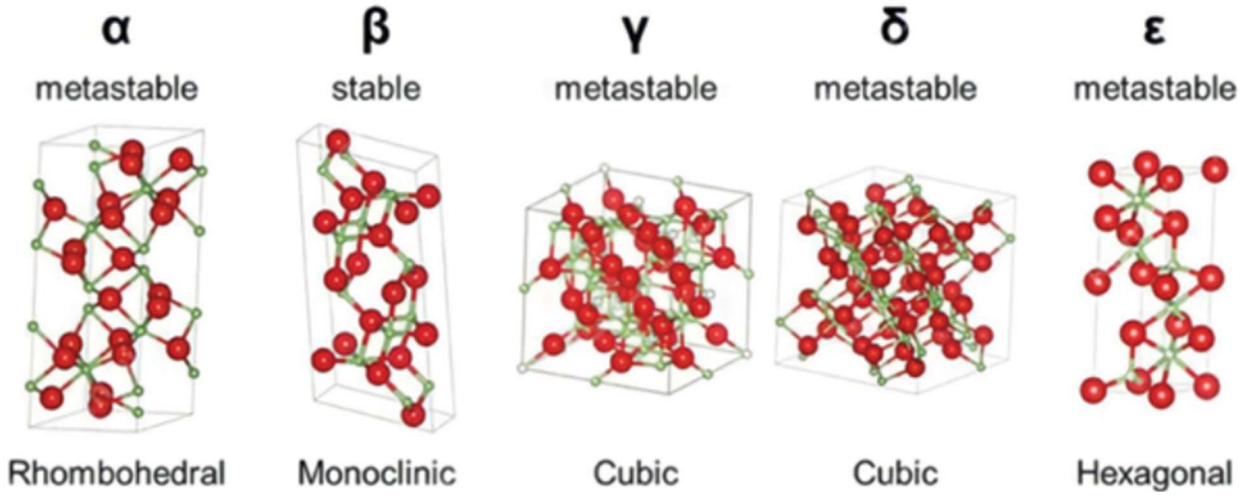

Figure 2: α-, β-, γ-, δ-, and ε-geometries of Ga_2O_3. These phases display rhombohedral, monoclinic, cubic, cubic, and hexagonal symmetries respectively [27]. α-, γ-, δ-, and ε-polymorphs are thermodynamically metastable because they transform to β-Ga_2O_3 at elevated temperatures of 700 °C.

sites and three inequivalent O sites (Figure 3). The Ga(I) atoms are tetrahedrally coordinated, while the Ga(II) atoms are octahedrally coordinated. The oxygen atoms are differently coordinated: O(I) and O(II) are threefold coordinated, while O(III) is fourfold coordinated [24]. One of β-Ga_2O_3's most attractive properties is its high breakdown field, estimated to be ~ 8 MV/cm, which surpasses most semiconductor materials. Many of the attractive properties of β-

Ga_2O_3 for electronics and high-voltage applications largely stem from its very wide bandgap. Beyond power electronics, β-Ga_2O_3 also shows promise in UV photodetectors, photocatalysts, flat-panel displays, UV filters, gas sensors, optoelectronic components, and biomedical devices [25-26, 28].

Similarly to ZnO, in micro- and nanoscale β-Ga_2O_3, both surface and bulk defects play crucial roles in determining the material's optoelectronic, chemical, and structural properties. The presence of inequivalent Ga and O lattice sites enhances interest in defect formation, as these sites exhibit different formation energies (as shown by the density functional theory calculations) leading to distinct vacancy and interstitial defect behavior [30-32]. At the free surface, such defects critically influence adsorption behavior, band bending, surface charge transport, charge recombination dynamics, photocurrent responses, and chemical reactivity [33-34]. β-Ga_2O_3 nanoparticles attracted interest for both antibacterial applications [35-40] and high-power electronic devices [28, 34]. For example, β-Ga_2O_3 demonstrates biodegradable properties under weakly acidic conditions, alleviating the issue of toxic accumulation in the human body [41]. Similar to micro- and nanoscale ZnO, ***the fundamental reasons for β-Ga_2O_3's antibacterial action mechanisms are unclear despite several studies on gallium-based antibacterials.***

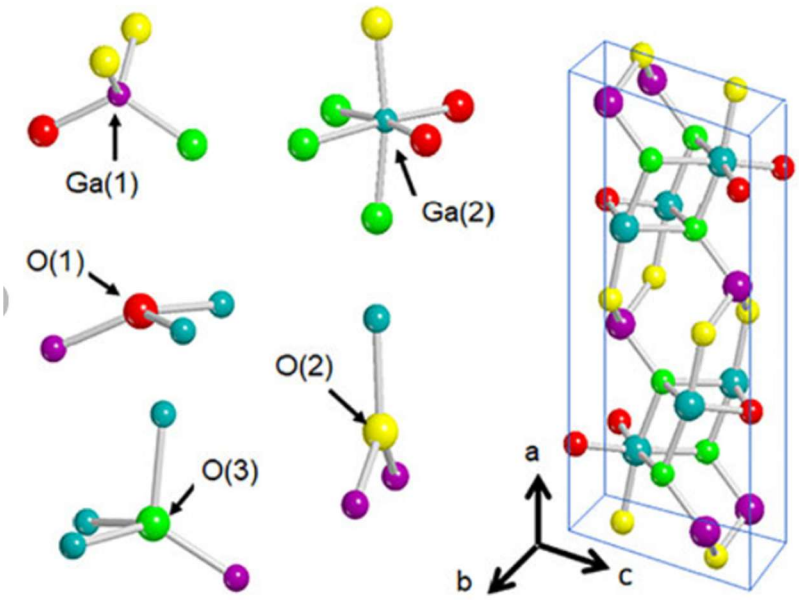

Figure 3: β-Ga_2O_3 monoclinic crystal structure illustrating inequivalent atomic sites, color-coded for clarity. Gallium atoms occupy two distinct coordination environments: Ga(I) = Ga(1) (tetrahedral) and Ga(II) = Ga(2) (octahedral). Oxygen atoms occupy three inequivalent sites, denoted as O(I) = O(1), O(II) = O(2), and O(III) = O(3) [29].

It is well known that β-Ga_2O_3 exhibits a persistent *n*-type conductivity [28, 30-31, 34, 42]. ***Understanding the fundamental mechanisms responsible for this behavior is essential to ultimately achieving a stable and reproducible p-type β-Ga_2O_3 material and thus a full utilization of this semiconductor in numerous potential applications*** [28,34,42].

Influence of Surface Stability of ZnO on its Antibacterial Properties

Several primary mechanisms have been proposed to explain the antibacterial activity of nanoscale ZnO against both Gram-positive and Gram-negative bacteria: cation toxicity [6, 14, 19, 20-21], generation of reactive oxygen species (ROS) [6, 14, 16, 20-22], direct cell rupture through surface-surface interactions involving exposed crystalline surfaces of ZnO [6, 14, 16-18, 20-23] and intra-cell internalization [6, 20-21].

Toxic cation ion release from the crystal free surface is one of the main mechanisms of ZnO's antibacterial action proposed by many sources [14, 18-19, 21, 43-47]. This mechanism occurs because Zn^{2+} has similar properties to Fe^{2+}, specifically the ionic 2+ charges and ionic radii of 74 pm and 76 pm respectively [35]. This gives Zn^{2+} ions biomimetic properties with well-established intra-cell penetration pathways [14, 43]. Zn^{2+} can appropriate the Fe^{2+} ion channels and subsequently replace Fe^{2+} during DNA transcription [14]. Zn^{2+} can interrupt not only the DNA transcription, but cellular functions associated with metabolic processes and enzymatic activities [18, 21, 44]. Johnson *et. al.* [48] reported on the influence of bacterial growth media on the antibacterial activity of Zn ions, indicating that cation ion release could become less effective over time during the interaction with media and bacteria.

ROS generation is suggested as another mechanism for ZnO's inhibition of bacterial growth, but this mechanism is still not fully agreed upon as mixed results have been observed. For ROS to occur, the ZnO surface would act as a catalytic interface, initiating a cascade of oxidation reactions that ultimately generate hydrogen peroxide (H_2O_2). It is still up for debate whether ultraviolet (UV) illumination must interact with the ZnO crystal for the reaction to occur [44]. The ROS generation (Figure 4) begins when dissolved oxygen molecules are reduced to superoxide radical anions (O_2^-•) via interactions with conduction electrons at the ZnO surfaces. These then react with protons (H^+) to form hydroperoxyl radicals (HO_2•). These intermediates can accept electrons to form hydroperoxide anions (HO_2^-), which are inherently unstable and subsequently react with protons to yield H_2O_2 [51-52]. Numerous reports addressed the role of ROS generation in the antibacterial action of ZnO micro-/nanocrystals. For example, in [53] the authors using gene expression from polymerase chain reactions (PCR) studied oxidative stress and changes in the relative fluorescence intensities of 2′,7′-dichlorodihydrofluorescein vs. H_2O_2 concentration [47]. On the other hand, in Caron *et. al.* [19], exposure of nanoscale ZnO crystal to *S. aureus* revealed that ROS generation – specifically H_2O_2 formation – did not contribute meaningfully to the observed antibacterial effects.

There have been experiments addressing the influence of surface-surface interactions between the ZnO crystalline surface and the bacterial cell wall. Xie *et. al.* [53] worked, using PCR testing, with the *Campylobacter jejuni* bacteria on ZnO to demonstrate nanoparticles' cell membrane permeability and damages to membrane

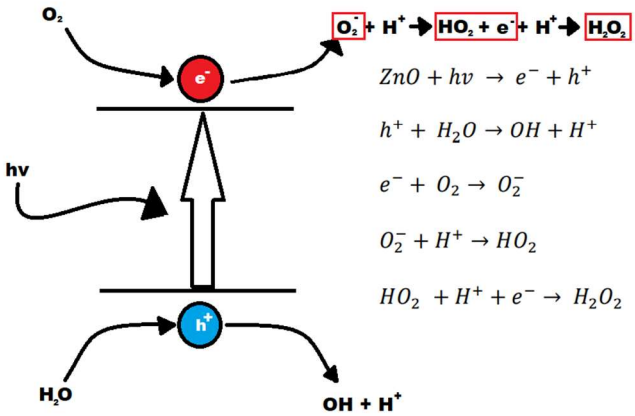

Figure 4: Schematic representation of reactive oxygen species (ROS) generation. More detail can be found in Refs. 51 and 52.

integrity. Furthermore, ZnO nanoparticles have been suggested [22] to create an electrostatic gradient difference across the negative membrane and the positive charges of the Zn^{2+} ions. On the other hand, Caron *et. al.* [19] achieved inhibition of *S. aureus* without any contact with ZnO nanoparticles, just through Zn^{2+} ion surface-defect mediated release from the ZnO surface. In this work it was shown that *S. aureus* inhibition increased with longer conditioning times, indicating that ZnO releases Zn^{2+} ions in a time-dependent manner that contributes to bacterial growth inhibition without direct contact. There were other studies of ZnO nanoparticles showing that cell membrane disruption is not necessary but quite impactful when allowable [22].

Cell internalization of nanoscale ZnO is an important antibacterial mechanism, as it entails interaction with the bacterial cell's internal components – DNA, lipids, proteins [21, 44], and metabolic pathways [21, 43]. E.g., *Staphylococcus aureus* cells are ~ 1 μm in size [49], making nanoparticle uptake possible. Adsorption of particles onto bacterial cell wall allows their internalization, which ultimately disrupts cell integrity by rupturing the cell wall or membrane [21, 44]. Particles with sizes <10 nm can pass through the cell plasma membrane and even transported into the cytoplasm of the bacteria [43]. To eliminate the impact of this phenomenon, in the earlier work of our group, Reeks *et al.* and Johnson *et al.* investigated microscale ZnO and still observed antibacterial activity, indicating that internalization is not a prerequisite for bacterial inhibition [14, 17-18, 50]. The enhanced toxicity of nanoscale ZnO relative to microscale forms has been consistently attributed to its higher surface area and reactivity rather than its capacity for internalization [45-46]. Consequently, the extent to which nanoparticle internalization contributes directly to antibacterial action remains uncertain.

It is necessary to further evaluate whether Zn^{2+} release promoted by surface defect serves as the primary antibacterial mechanism at the microscale. It was suggested in Ref. 54 that Fe, as a substitutional dopant in ZnO, may stabilize crystalline surfaces and thus affect Zn^{2+} release

behavior. Although the mechanisms by which Fe stabilizes ZnO surfaces remain unresolved, Fe doping has been theorized to suppress the internal dipole of ZnO and saturate dangling bonds on both polar and non-polar facets [54]. This stabilization is expected to limit the number of active sites available for Zn^{2+} leaching into the surrounding media. Conversely, Fe incorporation may introduce or enhance alternative antibacterial pathways, such as the Fenton reaction.

Our working hypothesis is that introducing an Fe dopant into ZnO will saturate surface defect sites – particularly on polar surfaces – thereby reducing Zn^{2+} release due to surface defect-mediated interactions and consequently decreasing bacterial inhibition relative to undoped polar ZnO. We will investigate microscale Fe-doped ZnO to be able to retrieve the particles and to compare pre- and post-assay properties of Fe:ZnO samples, thus excluding internalization as a mechanism.

Antibacterial Properties of Microscale β-Ga_2O_3 and GaOOH

β-Ga_2O_3 nanoparticles have garnered considerable attention for their antibacterial potential [35-38, 41, 56]. The predominant antibacterial mechanisms are generally attributed to toxic cationic (Ga^{3+}) release [38, 41, 55-56, 58], ROS generation [38, 55-57], and physical disruption of bacterial cell walls resulting from surface-surface interactions with the crystalline material [41, 56-57]. Additionally, nanoparticle internalization has been proposed as a contributing mechanism [35, 37-38, 56]. Gallium ions can also form complexes with organic compounds to generate hybrid antimicrobial materials, enhancing broad-spectrum efficacy, cellular targeting, and penetrability [41].

It has been reported that trivalent gallium ions (Ga^{3+}) can competitively substitute trivalent iron ions (Fe^{3+}), thereby disrupting essential biological processes. These include

metabolic pathways [38, 41, 56], DNA replication [55], and various enzymatic reactions – particularly those involved in bacterial resistance to ROS [38, 41]. This biomimetic behavior arises from the close similarity between Ga^{3+} and Fe^{3+} in terms of octahedral and tetrahedral ionic radii, as well as ionization potential [38, 41, 55, 58]. However, unlike Fe^{3+}, Ga^{3+} cannot be reduced under physiological conditions, leading to the interruption of redox-dependent bacterial processes and ultimately inhibiting cellular function [41, 55].

β-Ga_2O_3 has been hypothesized to generate ROS due to dissolved oxygen reacting with the surface of these nanoparticles. The ROS generated from the surfaces of these extracellular nanoparticles have been suggested to create superoxide radicals that can induce oxidative stress and compromise bacterial cell membranes [57]. Additionally, internalized nanoparticles of gallium have been shown to elevate intracellular ROS concentrations, causing damage to critical cellular components [56]. Compounding this effect, gallium ions have been demonstrated to disrupt bacterial ROS defense pathways, thereby amplifying oxidative damage. This dual-action mechanism – simultaneous ROS generation and inhibition of antioxidant defenses – likely contributes to the pronounced antibacterial potency of Ga-based nanomaterials.

Gallium ions can also combine with organic molecules to enhance broad-spectrum antibacterial performance. For instance, Xie *et al.* [41] synthesized indocyanine green-gallium (ICG-Ga) nanoparticles by mixing $GaCl_3$ with indocyanine green (ICG). Due to the incorporation of ICG, the resulting nanoparticles exhibited enhanced ROS generation under near-infrared (NIR) laser irradiation. Owing to their size, these nanoparticles were readily cleared by the kidneys, while biodistribution measurements revealed preferential accumulation in the liver of treated mice. This suggests the potential therapeutic applicability for hepatic bacterial infections [41, 58]. This integration of gallium ions with organic photoactive materials highlights a

promising strategy for engineering multifunctional antimicrobial nanoplatforms capable of combating multidrug-resistant bacteria in *in vivo* settings. [41, 59].

Gallium-based nanoparticles have been reported to interact with bacterial cell walls through surface–surface interactions involving their exposed crystalline surfaces. It has also been proposed that these nanoparticles can physically disrupt or tear bacterial membranes, with the extent of damage depending on their morphology. While β-Ga_2O_3 has previously demonstrated to have a strong correlation between particle morphology and antibacterial potency [35,41], gallium oxyhydroxide (GaOOH), a common precursor for β-Ga_2O_3 synthesis, has not been explored as an antibacterial agent. GaOOH is an inexpensive and well-defined crystalline product that can be synthesized hydrothermally and subsequently calcinated into β-Ga_2O_3 [61-62].

In our studies, we plan to establish a systematic framework for enhancing the antibacterial efficacy of β-Ga_2O_3 through controlled manipulation of its GaOOH precursor. Additionally, deeper investigation into the nature and dynamics of surface defect states in both GaOOH and β-Ga_2O_3 could provide critical insight into this lesser-recognized yet potentially significant antibacterial mechanisms. We will employ microscale particles to avoid internalization as an antibacterial mechanism and to have the ability to run comparative studies of pre- and post-assay samples.

The Role of Hydrogen Impurity in the Conductivity of β-Ga_2O_3

As an ultra-wide bandgap, the material β-Ga_2O_3 holds a strong potential as a reliable component in high-power electronic devices [28, 34, 42, 64]. However, achieving a β-Ga_2O_3-based homojunction, i.e., generating both an *n*-type and *p*-type material remains a significant challenge, limiting its applicability in devices [38, 64-65]. Consequently, the ability to precisely tailor electrical

and optical properties through a detailed understanding of the dominant electrically active point defects is crucial for advancing future electronic applications [64, 66]. As grown, β-Ga_2O_3 typically forms an unintentionally doped *n*-type semiconductor [67]. Moreover, β-Ga_2O_3 has the inherently flat valence band maximum (VBM) in momentum space for oxygen 2*p* states, which results in large effective hole masses and correspondingly low hole mobilities when *p*-type doping is attempted [42, 65, 67]. When β-Ga_2O_3 is scaled down to the micro- and nanoscale, surface defects start playing an increasingly dominant role in the electronic and structural properties of the material [68-69].

When examining the common non-impurity defects in β-Ga_2O_3, the primary intrinsic defects include gallium vacancies (V_{Ga}), oxygen vacancies (V_O), and Ga-O divacancies (V_{Ga} + V_O) [67]. In previous decades, the *n*-type conductivity of β-Ga_2O_3 has been attributed to the presence of V_O, largely based on the correlation between conductivity and oxygen partial pressure in annealing environments. However, Varley *et al.* performed theoretical calculations showing that V_O are deep donors in β-Ga_2O_3, resulting in ineffective contributions to free carrier generation [70].

Van de Walle employed DFT to model hydrogen-related defect states in ZnO, revealing that hydrogen acts as a nonamphoteric shallow donor stable across the entire Fermi energy range within the ZnO bandgap [71]. This theoretical prediction was later corroborated experimentally by Strzhemechny *et al.* confirming hydrogen's role as a pervasive shallow donor in ZnO [72]. The presence of such interstitial hydrogen complexes has since been recently proposed as a possible explanation for the intrinsic *n*-type conductivity observed in β-Ga_2O_3.

Hydrogen incorporation has been theorized and experimentally shown to affect the β-Ga_2O_3 electronic and charge carrier dynamics [73]. It particular, the theory predicts that both

interstitial and substitutional hydrogen forms shallow donors [74]. Specifically, interstitial hydrogen behaves exclusively as a shallow donor for any Fermi level within the band gap of β-Ga_2O_3 while substitutional hydrogen, H_O, has a low formation energy only under oxygen-poor conditions [70]. This leads to a high probability of H-decorated V_{Ga} formation that can be achieved after incorporating hydrogen into the crystal [65]. While cation vacancies typically exhibit high formation energies in many oxide semiconductors such as SnO_2, In_2O_3, first-principles DFT calculations have shown that formation energies of V_{Ga} are comparatively low in β-Ga_2O_3 [65]. Additionally, it has been calculated theoretically that the V_{Ga}-nH defect is energetically favorable compared to its V_{Ga} counterpart, along with its strong bonding that can resist temperatures as high as 1000 K [72]. ***In our studies, we plan to implement remote hydrogen plasma treatment to investigate primary mechanisms of n-type conductivity in β-Ga_2O_3 micro- and nanoparticles to evaluate potentially nonamphoteric behavior of hydrogen impurities.***

EXPERIMENTAL METHODS

Experimental techniques employed in this study range from microbiological to surface defect characterization. *One of our goals is to focus on the surface-defect mediated release of Zn and Ga ions into solution to provide further clarity behind ZnO and β-Ga_2O_3's antibacterial mechanisms.* In this regard, it is essential to monitor changes of both the bacterial growth dynamics and the impact on the crystalline surfaces, as both should elucidate each mechanism studied.

To quantify antibacterial action, we are using minimum inhibition concentration (MIC) assays. To synthesize ZnO and β-Ga_2O_3 microparticles, we are employing a bottom-up one-step hydrothermal method. To characterize our ZnO and β-Ga_2O_3 specimens, we use a variety of techniques as follows. The field-emission scanning electron microscope (FE-SEM) images the samples' morphology, which is then correlated with surface defect concentrations [17], optoelectronic processes [14], and inhibition of bacteria [46, 75]. Energy dispersive X-ray spectroscopy (EDXS) and inductively-coupled plasma – optical emission spectroscopy (ICP-OES) are used to identify bulk atomic stoichiometry. X-ray photoelectron spectroscopy (XPS) helps to identify surface composition and chemical bonding along with argon beam surface cleaning, a tilt-analysis method, and multiple anodes for depth-resolved studies [76]. Temperature-dependent Raman spectroscopy (T-Raman) and Fourier-transform infrared spectroscopy – attenuated total reflectance (FTIR-ATR) study vibrational modes to monitor quality of the samples and changes to surface and bulk structure. X-ray diffraction spectroscopy (XRDS) provides crystal lattice symmetry information and helps determine crystalline quality. To study optoelectronic properties of crystal defects, we utilize a combination of photoluminescence spectroscopy (PLS), energy-dependent surface photovoltage (ED-SPV) spectroscopy, and

thermoluminescence spectroscopy (TLS). We can additionally determine the bandgap energy of our materials via optical absorption spectroscopy. We use transient surface photovoltage (T-SPV) and impedance spectroscopy (IS) to study surface charge transport properties.

Our second goal is to investigate the role of H-doping in the persistent n-type conductivity of β-Ga_2O_3. For the synthesis of β-Ga_2O_3, we use a bottom-up hydrothermal synthesis for GaOOH production and furnace calcination to convert GaOOH into β-Ga_2O_3. To characterize the obtained materials, SEM, XPS, XRDS, T-Raman, and FTIR-ATR are employed. To dope β-Ga_2O_3 microparticles with hydrogen, we use inductively-coupled remote hydrogen plasma treatment. To study surface and bulk optoelectronic properties, we utilize optical absorption spectroscopy, PLS, TLS, radioluminescence (RL) spectroscopy and ED-SPV spectroscopy. To study charge transport, IS and T-SPV are employed.

Sample Synthesis

To synthesize ZnO and GaOOH, we utilize the same technique with certain modifications of reagents and growth parameters. β-Ga_2O_3 is obtained then through calcination of the GaOOH specimens.

ZnO and ZnO:Fe MPs are synthesized using the hydrothermal growth method. These microcrystals are grown from a 99.999% ethanol solvent with varied concentrations of $Zn(CH_3CO_2)_2 \cdot 2H_2O$ (zinc acetate dihydrate), $C_{19}H_{42}BrN$ (CTAB), and $Fe(NO_3)_3 \cdot 9H_2O$ (iron nitrate nonahydrate) depending on the targeted Fe doping concentration and crystal morphology required. These precursors are all mixed in the ethanol solvent, stirred until homogenous and fully dissolved into the solution. Because some of these reagents are not readily dissolved in a high-purity ethanol solvent, D.I. water is added until full dissolution. Following that, the wet

precursors are transferred into a Teflon tube container, which is then sealed within a stainless-steel autoclave reactor and placed into an AI Stabletemp forced air-drying oven. There the solution is subject to temperatures above 160°C for the reaction energy to be sufficient to crystallize ZnO. The reaction time varies depending on the desired morphology, generally between 18 hours and 26 hours. After this heat treatment, the resulting solution undergoes centrifugation and removal of the supernatant. The remaining solid is then washed and dried with D.I. water, acetone, and methanol. Adjustment of such parameters as relative precursor concentrations, temperature, reaction time, and pressure for synthesis of ZnO MPs are necessary for tunable size/morphology.

GaOOH MPs are synthesized similarly to ZnO and ZnO:Fe MPs via hydrothermal growth from a 60°C D.I. water solution containing 60 millimolar concentration of $Ga(NO_3)_3 \cdot 9H_2O$ (gallium nitrate nonahydrate). The initial pH of the solution is measured, then 1M NH_4NO_3 (ammonium nitrate) is added until the desired pH is reached. The homogenized solution is transferred into a Teflon tube container, sealed within a stainless-steel autoclave reactor and placed into an AI Stabletemp forced air-drying oven. There the solution is subject to a temperature of 140°C. The reaction in the oven proceeds for 10 hours. After this, the resulting solution undergoes centrifugation and removal of the supernatant. The remaining solid is then washed and dried with D.I. water, acetone, and methanol.

β-Ga_2O_3 is obtained from the synthesized and cleaned GaOOH product as follows. GaOOH is placed in an Al_2O_3 (aluminum oxide) open container crucible and transferred into a furnace preheated to temperatures between 800°C and 900°C. Calcination runs for 5 hours, after which the product is taken out of the furnace and allowed to cool.

Characterization Techniques

In the JEOL *field-emission scanning electron microscope* operating at 15 kV under a vacuum lower than 10^{-4} Pa (7.5×10^{-7} Torr), a collimated electron beam, emitted from a heated tungsten filament, is accelerated and focused onto the sample surface through a series of electrostatic and magnetic lenses. Upon interaction with the specimen, high-energy primary electrons penetrate the surface and generate a collision cascade, forming the characteristic teardrop-shaped interaction volume shown in Figure 5. The FE-SEM is equipped with a secondary electron detector that captures low-energy, inelastically scattered electrons originating from the surface and near-surface regions of the sample. The signal intensity is proportional to the number of detected secondary electrons, producing an SEM image that reveals surface morphology at magnifications down to the nanoscale.

Using the same JEOL FE-SEM instrument, *energy dispersive X-ray spectroscopy* (EDXS) measurements can be performed since the collision cascade produced by the high-energy incident electron beam can generate characteristic X-rays. These arise because of the electronic transitions between element-specific energy levels, providing unique spectral "fingerprints." By analyzing the energies and relative intensities of these emitted X-rays, both qualitative and quantitative compositional information can be obtained. Furthermore, by detecting backscattered electrons from the collision cascade we can correlate compositional data with surface morphology.

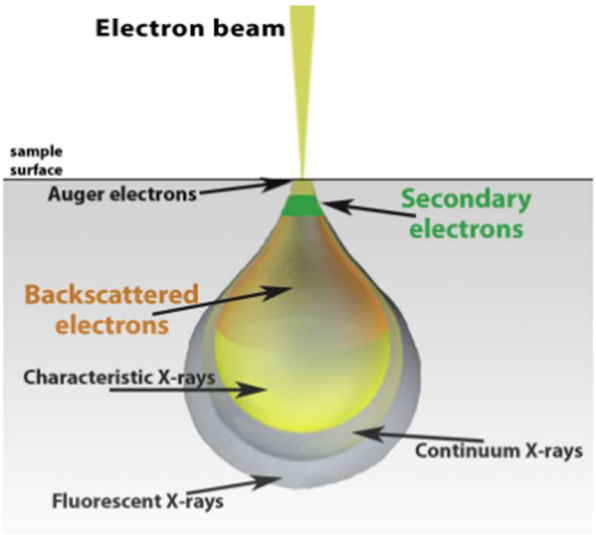

Figure 5: Schematic of electron beam producing a teardrop-shaped electron collision cascade [77].

This enables elemental mapping, where X-ray data are spatially overlaid on SEM micrographs, and allows for targeted compositional analysis of specific surface features or regions of interest.

X-ray diffraction spectroscopy (XRDS) is used to determine the crystallographic lattice structure of materials. In this technique, X-rays generated by high-energy electrons bombarding a metal anode are directed onto the sample. When these X-rays interact with the crystal lattice, they elastically scatter from it and produce diffraction patterns that follow Bragg's law of reflection. Constructive interference occurs at specific angles corresponding to particular crystallographic planes, resulting in characteristic diffraction peaks. By analyzing these peaks, the lattice structure and phase composition (amorphous, single-crystal, micro- or nanocrystal powders, etc.) of the material can be identified [78].

X-ray photoelectron spectroscopy (XPS) employs X-rays generated from a metal anode as the excitation source. When these X-rays irradiate the sample surface, they eject core-level electrons whose kinetic energies exceed the work function, allowing them to escape into the vacuum. Some of these electrons enter the hemispherical analyzer, where their kinetic energies are measured to produce an XPS spectrum. The spectral features include photoelectron lines, Auger peaks, and shake-up satellites. Because XPS is inherently surface-sensitive due to the limited escape depth of photoemitted electrons, it provides valuable information on the elemental composition and chemical states of atoms within the top few nanometers of the free surface [76, 79].

Inductively coupled plasma optical emission spectroscopy (ICP-OES) is an analytical technique used to determine the elemental composition of a sample with high sensitivity. In this method, the sample—typically in a liquid form—is introduced into a high-temperature argon plasma, where it is atomized and excited. The excited atoms and ions emit light at characteristic wavelengths as they return to lower energy states. This emitted light is dispersed radially and

axially and measured by a spectrometer, producing an emission spectrum where the intensity of each wavelength corresponds to the concentration of a specific element. ICP-OES is capable of detecting multiple elements at trace levels, making it a powerful tool for quantitative compositional analysis for detecting impurities.

Raman spectroscopy is an optical characterization technique that uses light scattering to study the vibrational modes and chemical bonds of a material. When monochromatic light interacts with a studied specimen, the scattered light can be divided into three main components: Rayleigh, Stokes, and anti-Stokes peaks. Rayleigh peaks correspond to elastically scattered photons with unchanged energy. Stokes peaks arise from inelastic scattering, where part of the photon's energy is transferred to lattice (or chemical bond) vibrations, producing scattered photons of lower energy. Conversely, anti-Stokes peaks occur when the lattice (or a chemical bond) is already in an excited vibrational state, resulting in scattered photons of higher energy than the incident light. The positions and intensities of the Stokes and anti-Stokes peaks reveal information about bond types and vibrational states within the material. In crystalline solids, these vibrational modes extend beyond individual bonds and are described as collective lattice vibrations, including both longitudinal and transverse optical and acoustic modes. Because Raman spectroscopy measures inelastically scattered light rather than absorbed light, only bonds capable of being polarized are Raman-active.

Fourier-transform infrared spectroscopy (FTIR) employs an infrared (IR) illumination source to excite vibrational modes within a sample. The IR spectral range is particularly significant because vibrational energy levels of chemical bonds fall within this region. Among the various modes of data collection, attenuated total reflectance (ATR) is commonly used to obtain FTIR spectra for surface and near-surface bonding information. In ATR-FTIR, the non-monochromatic source generates an evanescent wave that penetrates slightly into the sample

surface, allowing measurement of absorbance at different wavenumbers. The resulting maxima or minima in the spectra (depending on whether transmission or absorbance is recorded) correspond to the vibrational energies of specific bonds. Since IR absorption requires an interaction between the electric field and a changing dipole moment, only bonds that exhibit a dipole moment are FTIR-active. These vibrational energy levels provide valuable insight into the sample's composition, bonding environment, and structural purity. Raman and FTIR-ATR spectroscopy are considered complementary because they probe different types of vibrations: FTIR detects vibrations that involve a change in dipole moment, while Raman detects those that involve a change in polarizability. As a result, some vibrational modes may be active in one technique but not the other, allowing the two methods together to provide a more comprehensive understanding of molecular structure, bonding, and environmental interactions. Some vibrational modes can be active in both FTIR and Raman when they involve simultaneous changes in dipole moment and polarizability, whereas others may be inactive in both if they produce neither change, making them undetectable using these techniques.

Photoluminescence spectroscopy (PLS) is a technique for detecting optoelectronic signatures of crystal defects and other features of the electronic structure. In a PLS experiment, the sample is illuminated with light, inducing electronic excitations and subsequent radiative recombinations. In an ideal bulk semiconductor, emission arises only from band-to-band transitions at the bandgap energy. However, real crystals contain defects with electronic levels within the bandgap, leading to additional recombination events at lower energies. Thus, PLS reveals information about a material's electronic energy structure, including bandgap energy and the relative positions of defect states. Performing PLS as a function of temperature provides further insight, as variations in peak position, intensity, and linewidth reflect fundamental interactions and defect dynamics within the lattice.

Thermoluminescence spectroscopy (TLS) operates on a similar principle but uses heat instead of light to stimulate recombination. As the temperature increases, trapped charge carriers are thermally released and recombine radiatively, producing luminescence over time. The thermal excitation modifies carrier distributions according to the Fermi-Dirac function, enabling analysis of recombination kinetics and defect energetics. By examining the evolution of luminescence intensity and photon energy with temperature, TLS provides complementary insight into the electronic structure and defect-related processes of the material.

Surface photovoltage (SPV) is a contactless technique used to study how the material's surface work function and surface potential respond to illumination. Specifically, the response can be measured as a function of time (T-SPV) or as a function of the wavelength or photon energy of the incident light (ED-SPV spectroscopy). The measurement employs a non-contact, oscillating electrode known as a Kelvin probe, positioned near the sample surface. A small current is established between the probe and the sample, and variations in surface charge distribution or band bending induced by illumination alter the contact potential difference between them. These changes in potential provide information about charge separation, surface states, and carrier dynamics at or near the surface of the material.

Impedance spectroscopy (IS) is a technique in which an alternating current is applied across a sample over a range of frequencies to measure its complex impedance. The resulting phase difference between the applied current and the measured voltage allows the material to be modeled as a combination of resistive and capacitive components. This frequency-dependent response allows modelling of charge transport and relaxation dynamics within the material. It is particularly useful for studies of pelletized micro- and nanopowders because the interactions between surfaces become dominant, altering the mechanisms of conduction. Performing IS measurements as a function of temperature further reveals how charge transport mechanisms

evolve with temperature, specifically the influence of such factors as carrier mobility and trap states.

Minimum Inhibition Concentration Assays

We evaluate the antimicrobial activity of our oxide specimens in a controlled environment to assess their ability to kill or inhibit growth of bacteria. The bacteria are exposed to oxides during the logarithmic growth phase (the period of maximum population increase) to assess whether the presence of the micro- and nanoparticles inhibits bacterial proliferation. The bacterial cultures and oxide samples are co-incubated under standard conditions for 18-22 hours using a vertically rotating holder to maintain uniform suspension.

Following incubation, the mixture of bacteria, growth medium, and oxide particles are analyzed spectroscopically by measuring the optical density at 600 nm (OD_{600}). A higher absorbance value corresponds to greater bacterial growth. By comparing OD_{600} values across varying oxide concentrations, one constructs a dose-response curve to determine the relationship between particle concentration and bacterial inhibition or killing efficiency.

RESULTS AND DISCUSSION

Results for ZnO and ZnO:Fe

The previously described hydrothermal synthesis yields micro- and nanoscale ZnO particles. SEM images in Figure 6 show submicron undoped ZnO particles. Figures 7 and 8 provide both quantitative confirmation and qualitative evidence of successful Fe incorporation into the ZnO lattice. In particular, ICP-OES results (Figure 8) show that the measured Fe content falls somewhat below the theoretical targets but shows an intended trend of increasing concentrations. The tendency for lower experimental values would require further investigation and optimization of reagent concentrations to achieve the desired doping levels. Nevertheless, the current data demonstrates a positive outcome for a consistent increase in Fe incorporation within ZnO during synthesis.

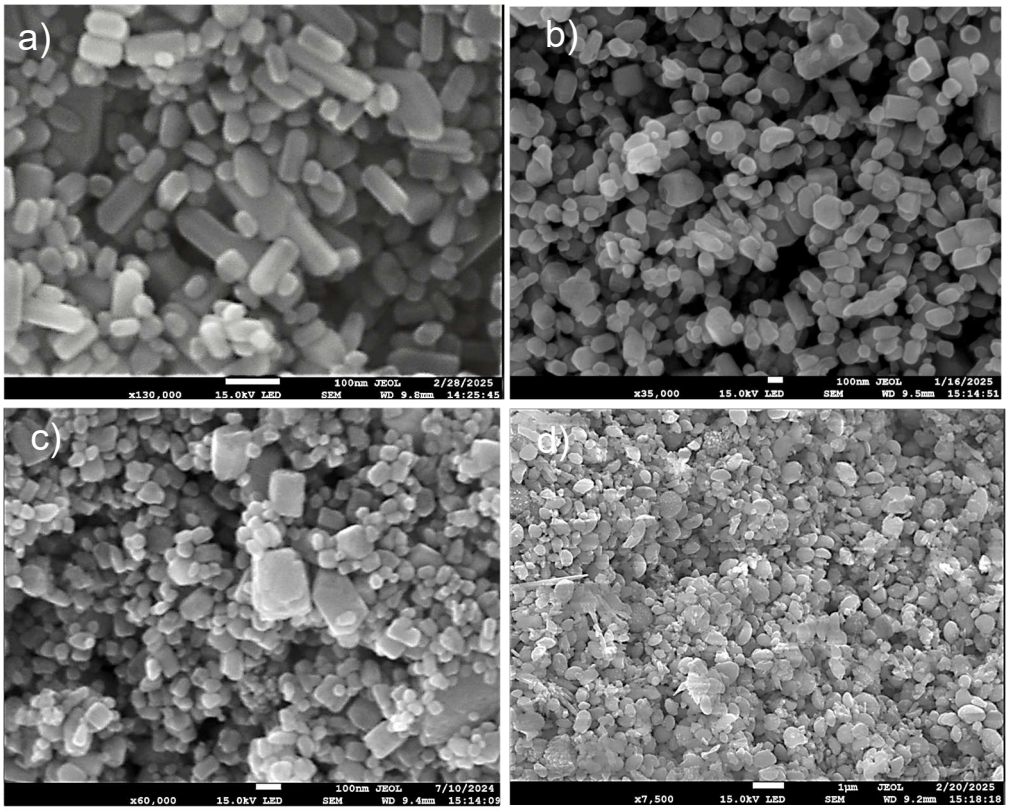

Figure 6: SEM images of hydrothermally-grown ZnO particles: (a) undoped, (b) 1% Fe-doped ZnO, (c) 2% Fe-doped, and (d) 3% Fe-doped ZnO.

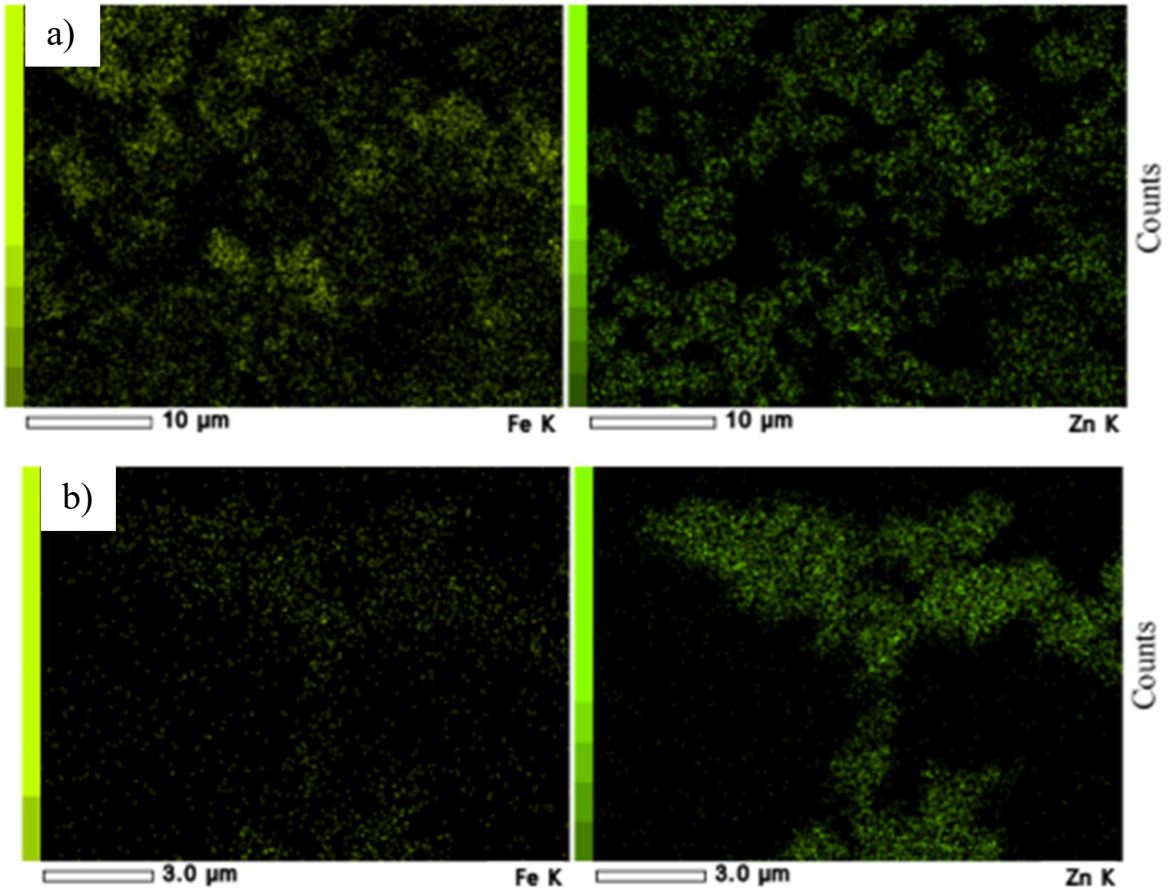

Figure 7: EDXS elemental maps showing qualitative differences between (a) 9% Fe-doped ZnO and (b) 2% Fe-doped ZnO samples. Based on intensity mapping, a general increase in Fe incorporation within the ZnO crystals is observed with higher $Fe(NO_3)_3$ concentrations during synthesis.

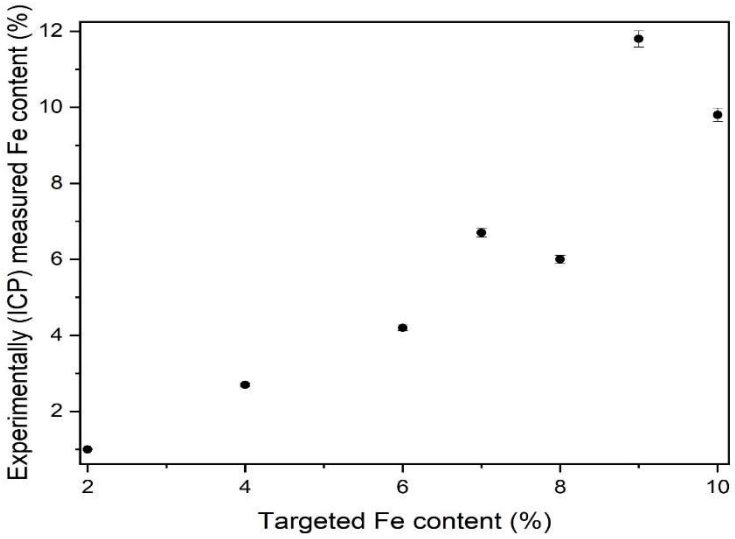

Figure 8: ICP-OES data showing the experimentally measured Fe-doping concentrations in ZnO compared to the theoretical target values. Error bars represent the percentage error determined from the calibration step of the ICP-OES measurement.

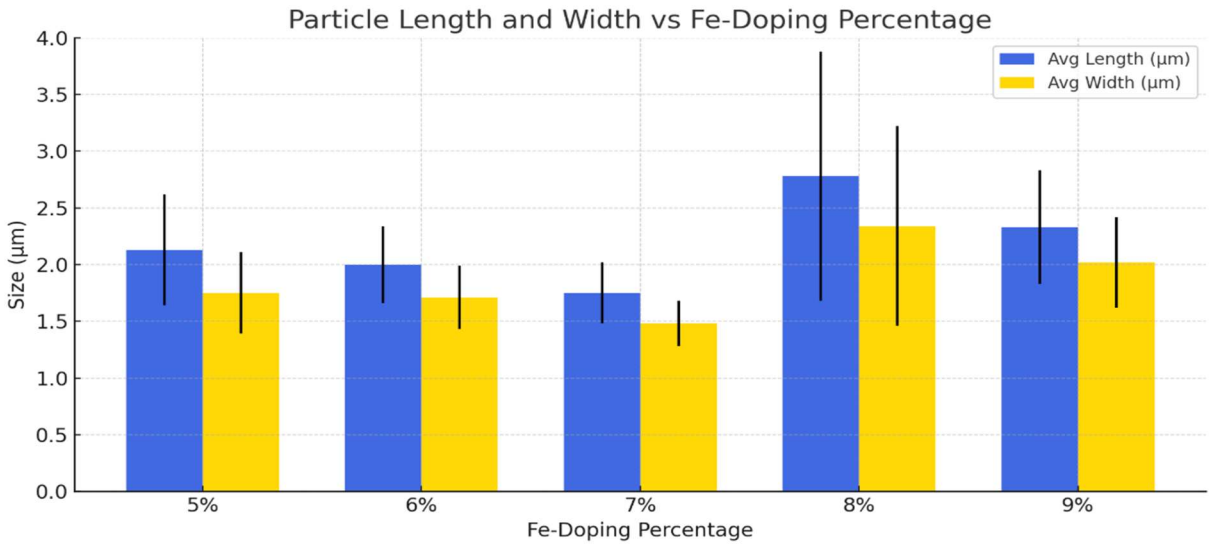

Figure 9: ImageJ-based size analysis performed using SEM images of Fe-doped ZnO samples. Average particle lengths and widths were measured. Error bars represent the smallest and largest particle dimensions observed within each sample.

The literature commonly reports a reduction in particle size of the Fe-doped ZnO particles relative to undoped ZnO. In contrast, our results (Figures 6 and 9) indicate that increasing Fe doping leads to either a comparable or slightly larger average particle size. This was observed in SEM images via ImageJ analysis of long-axis and short-axis measurements across 100+ particles for average length and width respectively. Additional synthesis iterations under controlled conditions will be necessary to confirm this trend. We suggest that this happens due to the use of a pure ethanol solvent rather than a pure D.I. water solvent during synthesis. Figure 6 reveals that the current synthesis produces a mixed particle morphology, which at present limits our ability to isolate the effects of polar versus non-polar surface contributions. To better investigate these surface-dependent effects, syntheses will need to be tailored in the future to yield samples with distinct polar/non-polar surface abundances.

The crystalline quality of our samples is illustrated in Figures 10 and 11. The XRDS and T-Raman spectra provide information on the lattice structure and phonon modes of the material, respectively. These spectra confirm that our synthesis yields high-quality ZnO crystals, despite

the somewhat irregular morphology observed in Figure 6a. Upon introducing Fe dopants, the XRDS patterns (Figure 10) indicate that the wurtzite lattice structure is maintained up to 10% Fe incorporation. In contrast, the T-Raman spectra (Figure 11) reveal a decrease in the intensity of the E_2^{High} phonon mode. Since Fe is slightly less massive than Zn, substitution of Zn^{2+} ions with Fe^{2+} ions introduces mass irregularities that dampen some lattice vibrations.

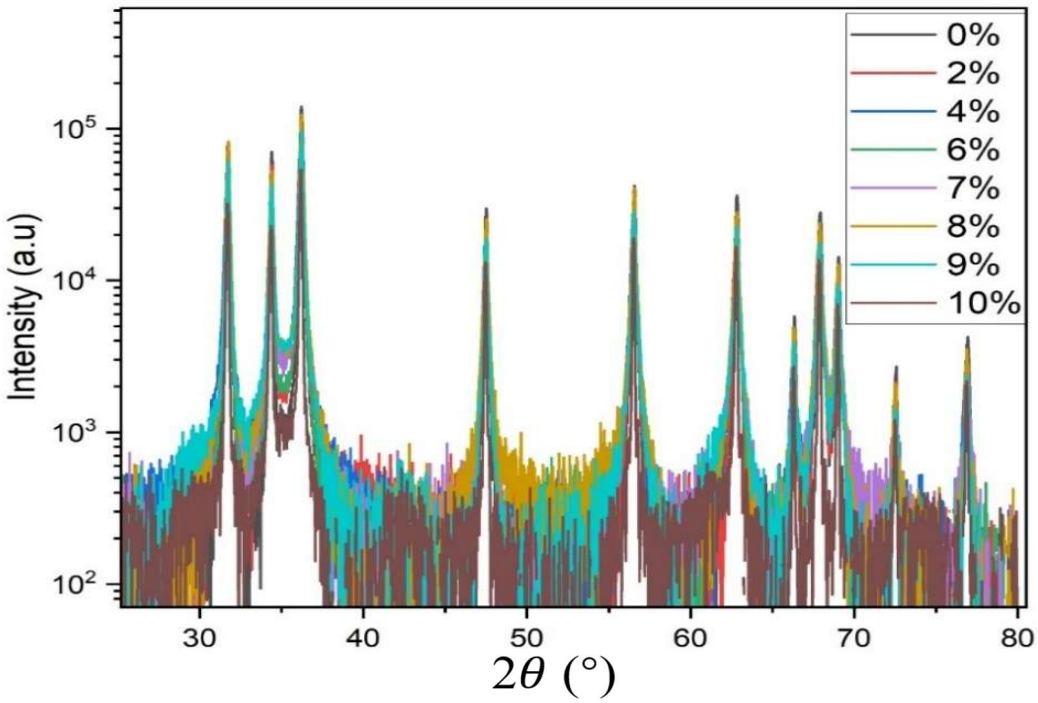

Figure 10: XRD spectra of ZnO particles with varying Fe doping concentrations. These results show a hexagonal wurtzite pattern for all doping levels up to 10%. There was no presence of secondary phases.

Optical absorption measurements (Figure 12) show the emergence of a new absorption band in the near-infrared (NIR) region with Fe doping, consistent with increased Fe incorporation into the ZnO lattice. No such absorption is observed for the undoped ZnO sample.

Optical absorption measurements in the UV region (Figure 13a) show that increasing Fe doping concentration results in a consistent redshift of the bandgap energy. Taking the derivative of Figure 13a leads to Figure 13b, associating peak position with energy values. Figure 14 emphasizes how this peak position from Figure 13b changes due to doping concentration of Fe. The ZnO bandgap transitions arise between the valence band maximum (VBM), primarily

composed of O 2*p* orbitals, and the conduction band minimum (CBM), dominated by Zn 4*s* orbitals, as discussed in the Introduction. Theoretically, substitution of Zn^{2+} ions with Fe^{3+} ions disrupts this electronic configuration, which in return could result in narrowing the bandgap and shifting the optical absorption edge toward lower energies.

To further probe the impact of Fe doping on surface defect states, PLS was employed. PL spectra in Figure 15 indicate that the primary recombination mechanisms associated with trap-state transitions and direct CBM-VBM transitions remain largely unchanged with the introduction of 2% Fe. Here, in the normalized PL curves both the defect-related and near-band-edge emissions exhibit comparable relative intensities. However, the increased noise observed for the 2% Fe-doped indicates a reduced intensity of the signal compared to the 0% Fe-doped sample, implying a reduction in radiative recombination efficiency because of the increased probability of non-radiative mechanisms.

Antibacterial assays are still ongoing to fully evaluate the antibacterial activity of the synthesized particles; however, preliminary data are presented in Figures 16 and 17 indicating that both undoped ZnO and 3% Fe-doped ZnO crystals exhibit inhibitory effects against *S. aureus* at a concentration of 5 mg/mL. It should be noted, however, that these findings lack reproducibility across trials, as displayed in Figure 17a, suggesting that surface or morphology characteristics of the particles may play a role in diminishing antibacterial efficacy. While this variability in MICs does not invalidate the results shown in Figure 16, it emphasizes the need for further investigation into the factors influencing this variability. Establishing a reproducible antibacterial baseline for undoped ZnO is essential before determining whether Fe incorporation amplifies or suppresses antibacterial activity through modifications of surface chemistry or bulk properties.

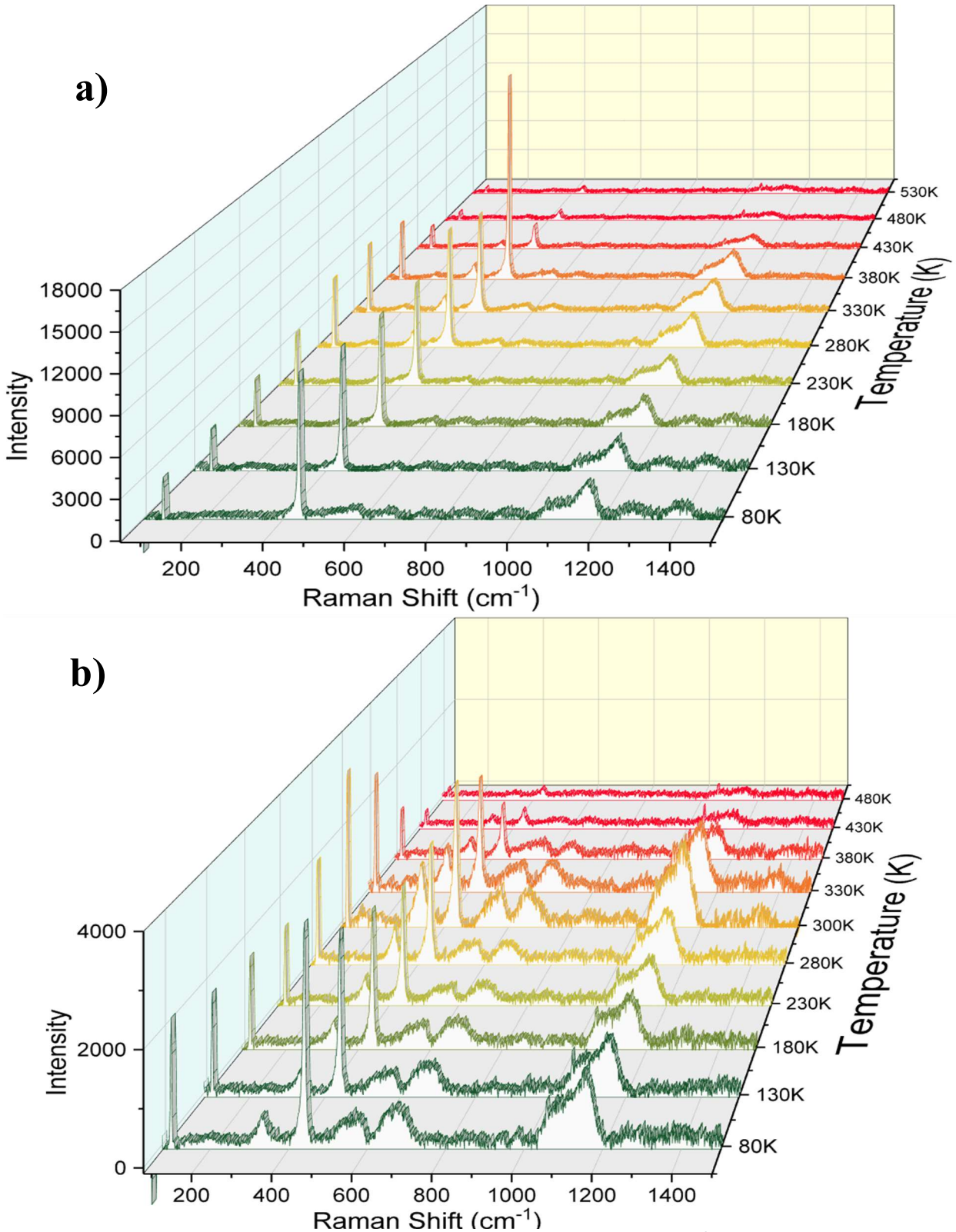

Figure 11: T-Raman spectra for (a) undoped ZnO sample and (b) 2% Fe-doped ZnO sample. E_2^{High} relative peak intensity at ~437 cm^{-1} changes with Fe concentration.

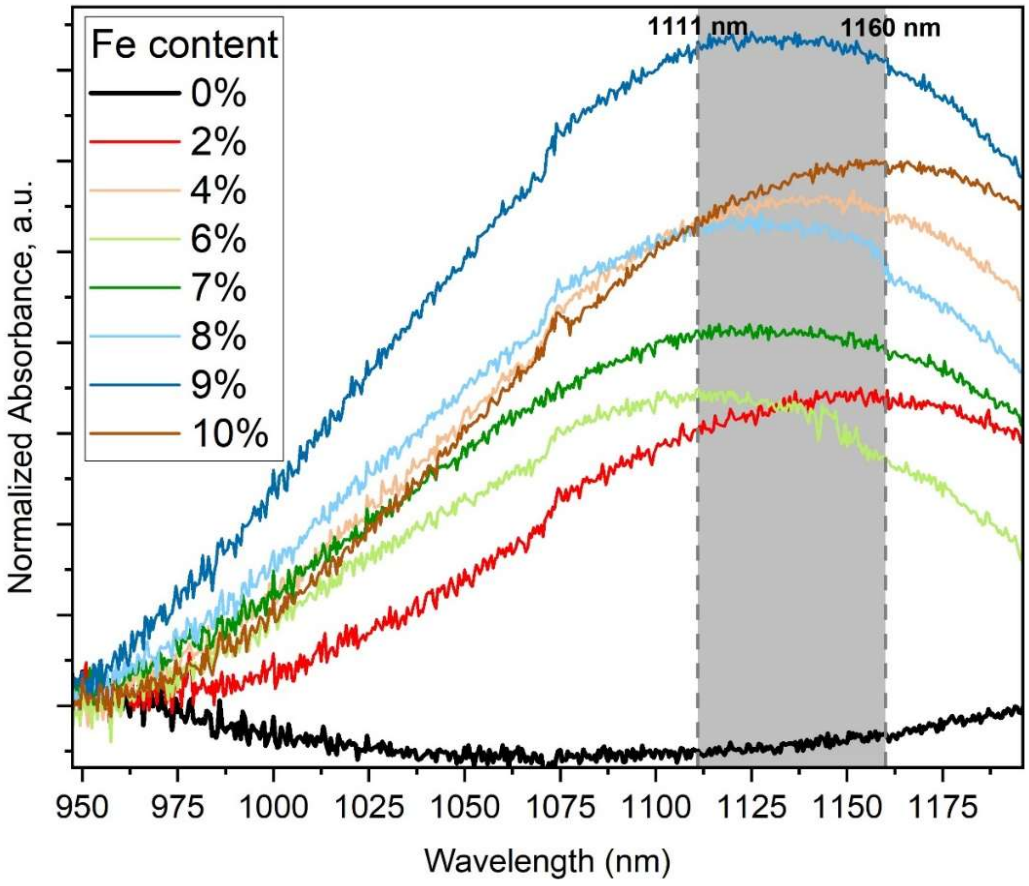

Figure 12: NIR optical absorption spectra of ZnO microcrystals with varying Fe doping concentrations. This band forms due to the incorporation of Fe into the ZnO lattice. Gray area emphasizes areas including peak maxima from all doped samples.

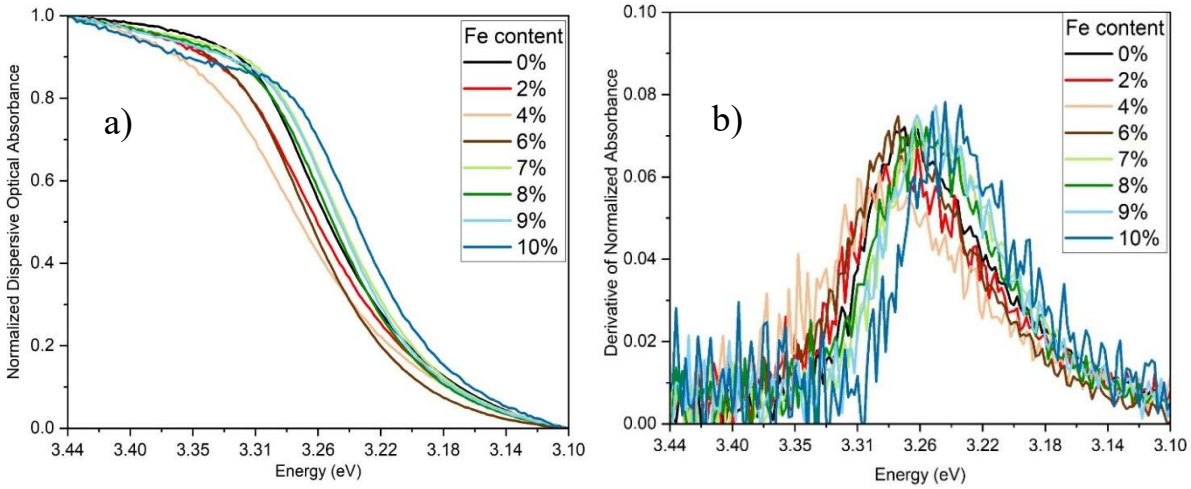

Figure 13: (a) UV optical absorption spectra of ZnO microcrystals varying Fe doping concentrations. (b) Derivative of the spectra in (a) indicating change of the bandgap energy with Fe doping levels.

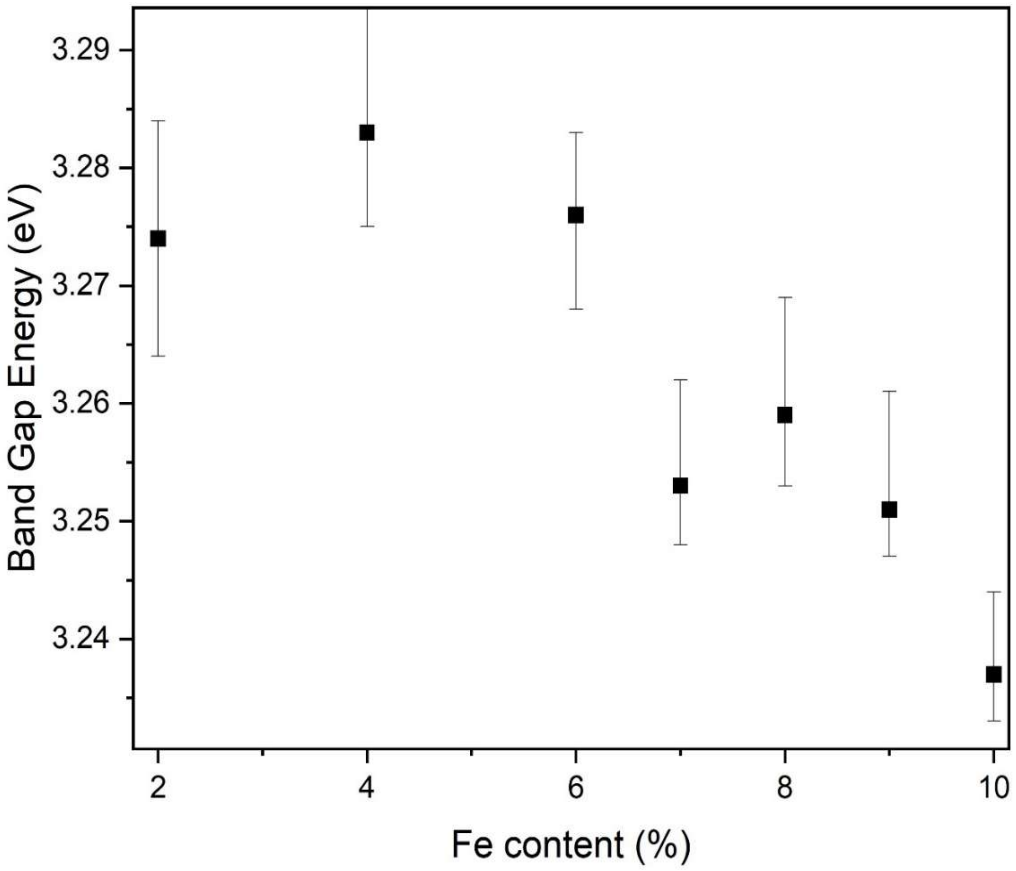

Figure 14: Peak positions extracted from Figure 8b), highlighting the functional dependence of the bandgap energy vs. Fe doping concentration in ZnO. The upper and lower error bars represent the range between the highest and lowest credible peak positions determined from the same dataset.

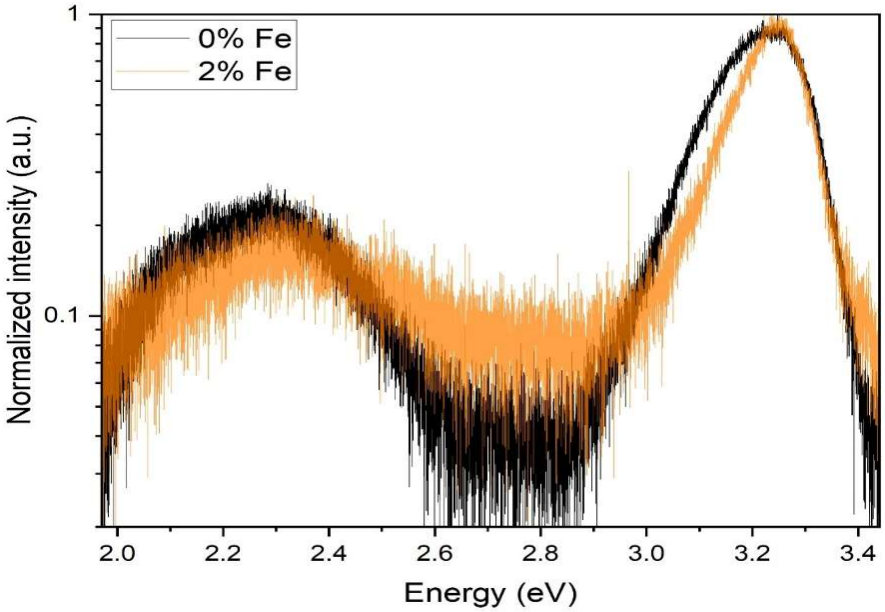

Figure 15: Normalized PL spectra comparing undoped ZnO and 2% Fe-doped ZnO samples. The 2% Fe-doped ZnO sample exhibits a lower overall emission intensity relative to the undoped ZnO, indicating reduced radiative recombination efficiency. The ratio between the near-band-edge and defect-related emission peaks remains consistent between the two samples.

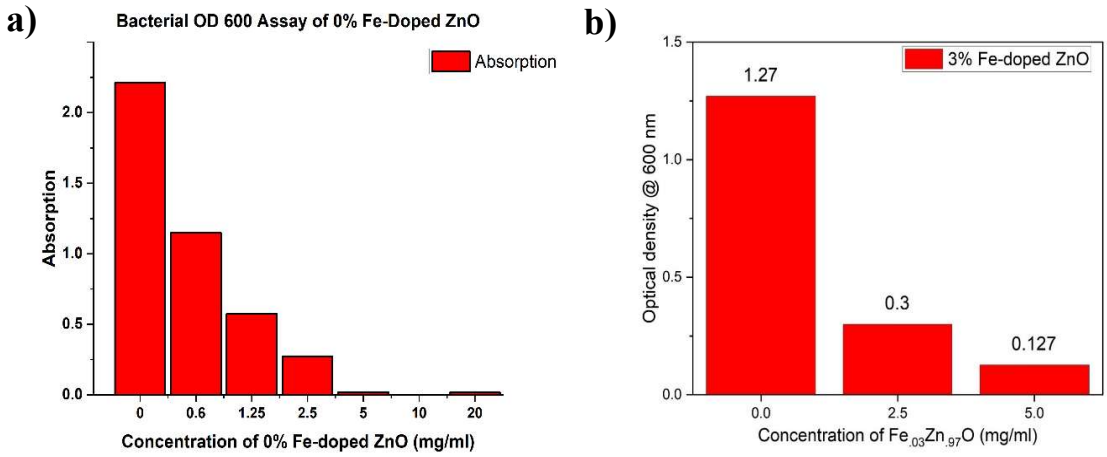

Figure 16: Minimum inhibitory concentration (MIC) assays against S. aureus for (a) undoped ZnO and (b) 3% Fe-doped ZnO samples. Both samples exhibit an MIC of 5 mg/mL, indicating minimal change in antibacterial activity with light Fe doping.

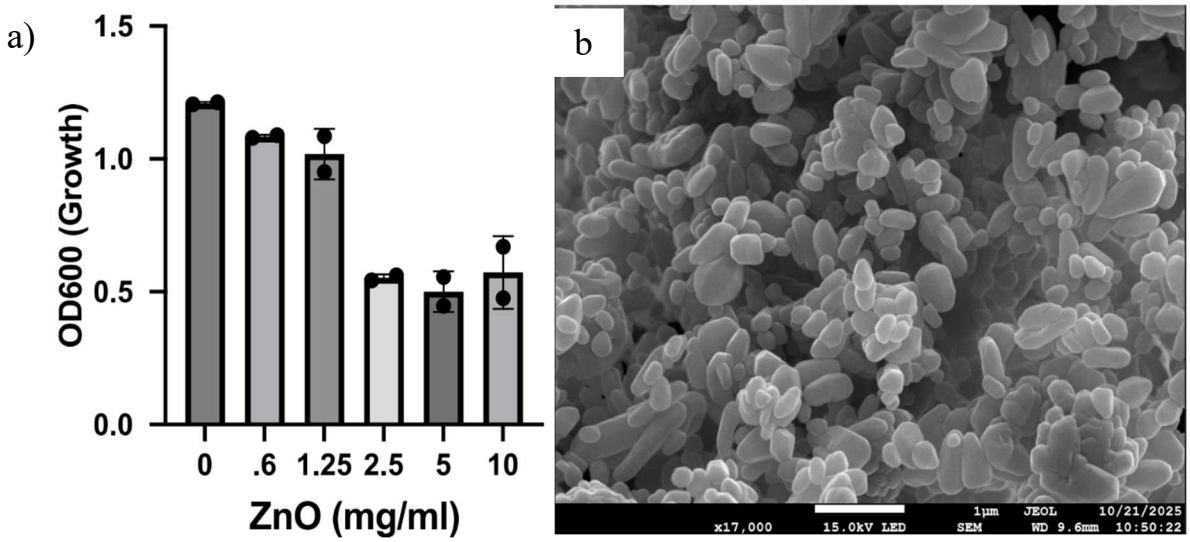

Figure 17: (a) Minimum inhibitory concentration (MIC) assay against S. aureus of an n=3 data set for the lab-grown 0% Fe-doped ZnO displayed in on the right. (b) lab-grown 0% Fe-doped ZnO samples in pure ethanol solution at 0.10M $ZnAc_2 \cdot 2H_2O$ and 0.01g CTAB. Sample was placed in oven at 180℃ for 24 hours and cleaned with methanol, D.I. water, and Acetone.

Results for GaOOH

In [60] we investigated GaOOH microparticles to address the relationship between surface defects, morphology, and bacterial inhibition against *S. aureus* and *Escherichia coli* (*E. coli*). In this study, variation of the synthesis pH was found to modulate both the morphology and the abundance of surface defect sites on GaOOH microparticles. We found a relationship between antibacterial inhibition and the concentration of surface defects in the GaOOH microparticles. Our findings, discussed in this section, underscore the role of surface-defect-mediated interactions in governing the antibacterial behavior of gallium-based oxide materials.

GaOOH microparticles were synthesized via the hydrothermal growth method described above, with the pH of the precursor solution at 6, 7, 8, 9, 9.5, and 10. SEM imaging (Figure 18) was used to examine morphological changes as a function of pH. As the solution pH increases from 6 to 10, the morphology transitions from well-defined rhombohedral microrods to more layered structures. This evolution is attributed to the increasing concentration of hydroxyl ions in the growth environment, coupled with the action of NH_4OH generated during synthesis, which functions both as a reducing agent and a capping ligand [77].

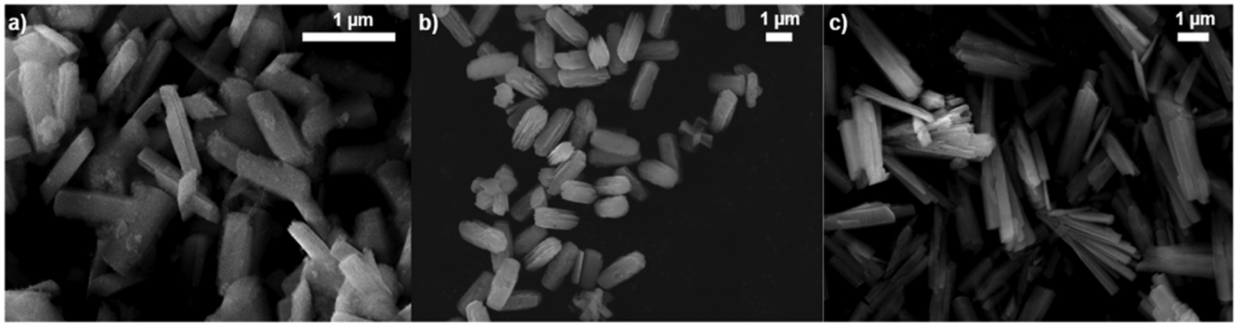

Figure 18: SEM images of GaOOH grown with a varying pH of synthesis solution (a) pH 5, (b) pH 8, and (c) pH 10.

Figure 19 highlights the strong dependence of microrod length on synthesis pH, demonstrating a clear trend of increasing particle length with increasing pH. Specifically, samples synthesized at pH 10 exhibit microrods nearly four times longer than those produced at pH 6. This behavior likely arises from preferential adsorption of hydroxyl groups on crystal

facets along the *c*-axis, promoting anisotropic growth [81]. The nonlinear relationship between particle length and pH can further be explained by the logarithmic dependence of pH on the concentration of OH^- species in solutions.

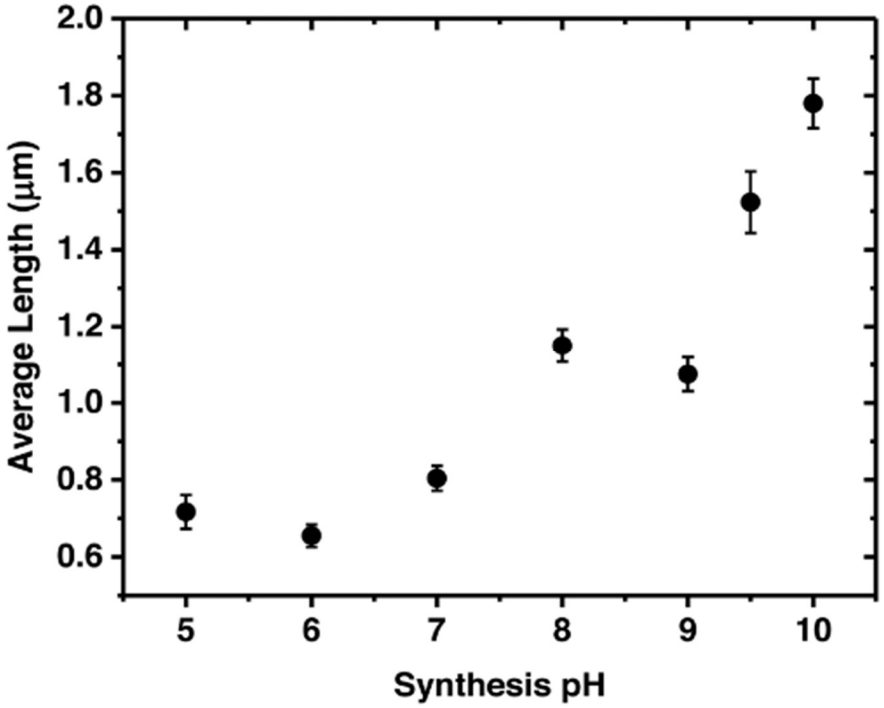

Figure 19: Average length of hydrothermally grown GaOOH microparticles as a function of synthesis pH. Data represents the mean standard deviation (SD) calculated from measurements of more than 35 particles per sample.

XRDS was used to investigate crystallinity and confirmation of lattice structure. The intensity and sharpness of the peaks in Figure 20 indicates the presence of highly ordered (110) and (111) lattice planes characteristic of good-quality GaOOH crystals [78, 82].

To evaluate the antibacterial efficacy of GaOOH microparticles, inhibition assays were conducted using *S. aureus* and *E. coli* (Figure 21). Despite previous reports suggesting that GaOOH can reduce the antibacterial efficacy of other compounds [38,83], our results reveal that GaOOH microparticles possess a direct antimicrobial effect. This finding is particularly noteworthy as it represents the first direct demonstration of such behavior in microscale GaOOH particles, which are too large to be internalized by bacterial cells, implying that the mechanism

likely involves either surface interactions or the release/generation of bactericidal molecular or ionic species.

Furthermore, the assays revealed differential bacterial inhibition, with GaOOH exhibiting greater activity against the Gram-positive *S. aureus* than the Gram-negative *E. coli*. This disparity may arise from structural differences in the cell walls; Gram-negative bacteria possess an outer membrane that limits the penetration of external agents, unlike Gram-positive bacteria, which lack this additional barrier [84]. For *S. aureus*, strong cytotoxic effects were observed across all GaOOH morphologies, making it difficult to distinguish between shape-dependent behaviors as seen in Figure 21b. In contrast, the *E. coli* assays seen in Figure 21a demonstrated enhanced inhibition by GaOOH microparticles synthesized at higher pH values, suggesting that synthesis conditions play a key role in modulating antibacterial performance.

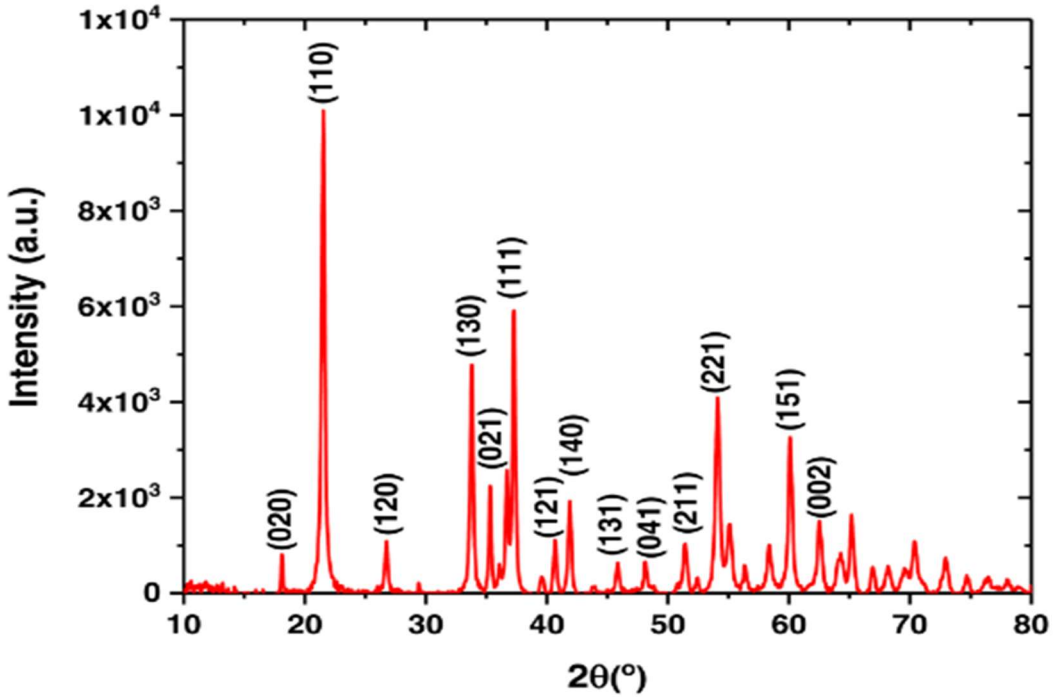

Figure 20: XRD spectrum of GaOOH microparticles synthesized with pH 7 of the precursors.

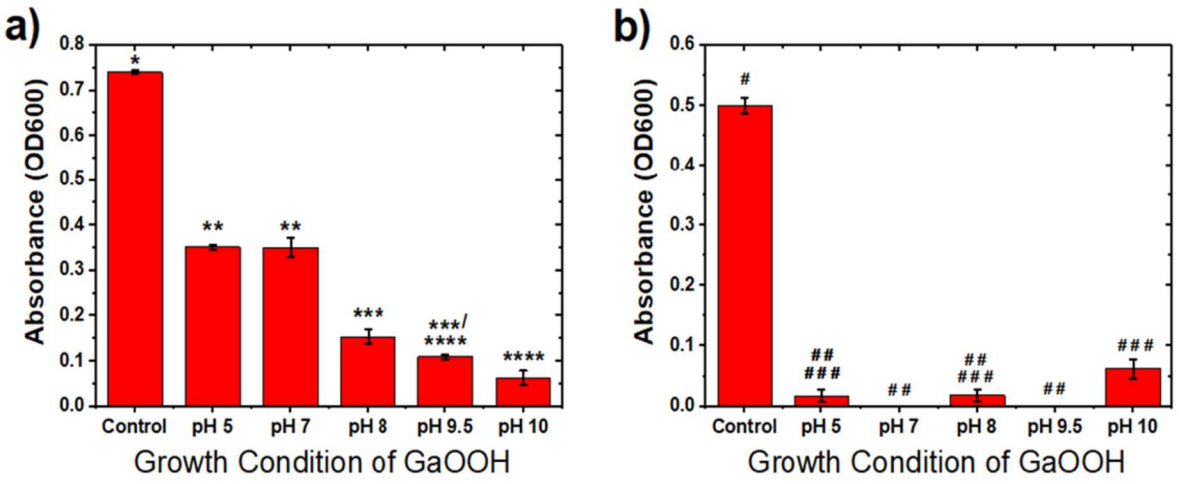

Figure 21: Optical density measurements from bacterial inhibition assays performed with 5 mg/ml concentration of GaOOH solutions against (a) E. coli and (b) S. aureus. Data are presented as mean standard deviation (SD) from three independent trials. Statistical significance was determined using one-way analysis of variance (ANOVA) followed by Tukey's Honestly Significant Difference (HSD) post hoc test ($p < 0.05$). Distinct statistical groups are indicated by (a) asterisks (*) and (b) number signs (#), respectively.

We conducted PL experiments to elucidate how synthesis pH influences optoelectronic properties of GaOOH microparticles. It has been proposed that surface defects can lead to leeching of Ga^{3+} ions into media, allowing for biomimicry of Fe^{3+} as described earlier in the Introduction. This mechanism, along with increased vulnerability to ROS generation and enhanced surface-surface interactions, could be driven by surface defects, which have been shown to play key roles in the antibacterial performance of other oxides [14]. It is well established that both the intensity and position of PL peaks in GaOOH vary with synthesis conditions, including pH, as these parameters influence defect density and distribution [85]. Typically, GaOOH exhibits broad PL emission bands spanning the visible to near-UV range, corresponding to various radiative recombination processes within the material. The lower-energy emissions are generally associated with intrinsic defects such as oxygen vacancies, gallium interstitials, and hydroxyl-related states [82, 86]. The PLS of GaOOH microparticles synthesized at different pH values (Figure 22a) were normalized using the maximum of the near band-edge (NBE) peak at approximately 3 eV.

In Figure 22b we present the ratio of the intensities of the defect-related emission band at approximately 2.4 eV to that of the NBE peak, plotted as a function of synthesis pH. One can see that the synthesis pH of GaOOH microparticles strongly influences their PL characteristics, with higher pH values promoting enhanced defect-related emission. The increase in defect band relative intensity corresponds to a higher defect density in samples grown under more basic conditions. This finding provides context for the observed antibacterial behavior, as more defective crystals likely offer a greater number of interaction sites for bacterial contact or medium components and may exhibit reduced structural stability, potentially facilitating the release of Ga^{3+} ions with known toxic and biomimetic activity.

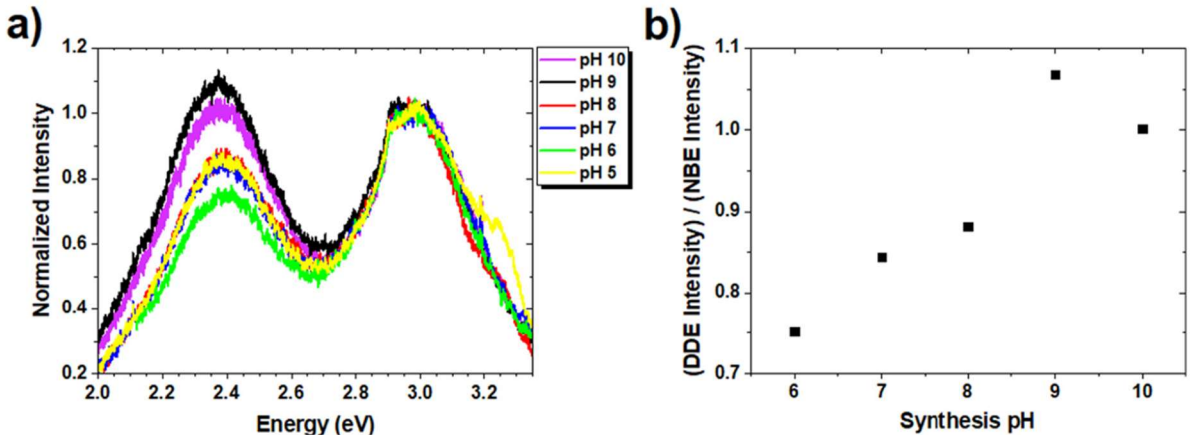

Figure 22: (a) PL spectra of hydrothermally grown GaOOH microparticles synthesized with varying pH values, normalized to the near band-edge (NBE) emission peak maximum. (b) Ratio of the defect-related peak (~ 2.4 eV) intensity to the NBE emission band plotted as a function of synthesis pH.

FTIR-ATR results presented by Figure 23 show the vibration absorption in the GaOOH microcrystals. These sharp minima near 1000 cm^{-1} are attributed to Ga-O (lower frequency) and Ga-OH (higher frequency) bending vibrations, characteristic of the GaOOH crystal structure. From Figure 23c and Figure 23d one can see that the synthesis pH selectively influences the Ga-OH bending frequency, and not the Ga-O bending mode, with the latter originating from the more stable core structure of GaOOH. The Ga-OH vibrations are more sensitive to surface-specific modifications, such as increased hydroxyl incorporation, hydroxyl deprotonation, or the

formation of defect sites that introduce local strain and structural distortion. The increased likelihood of defect formation aligns well with the observed changes in SEM morphology, the trends in PL defect emission, and the results of the antibacterial assays [60].

To further quantify contributions of defects in GaOOH microparticles to antibacterial action, future work should employ surface photovoltage (SPV) and high-resolution PL analyses. These techniques would enable identification of the surface states in relation to synthesis pH. Beyond characterization of GaOOH, the same particles can be calcinated into β-Ga_2O_3 and examined under equivalent conditions to study defect-related antibacterial mechanisms.

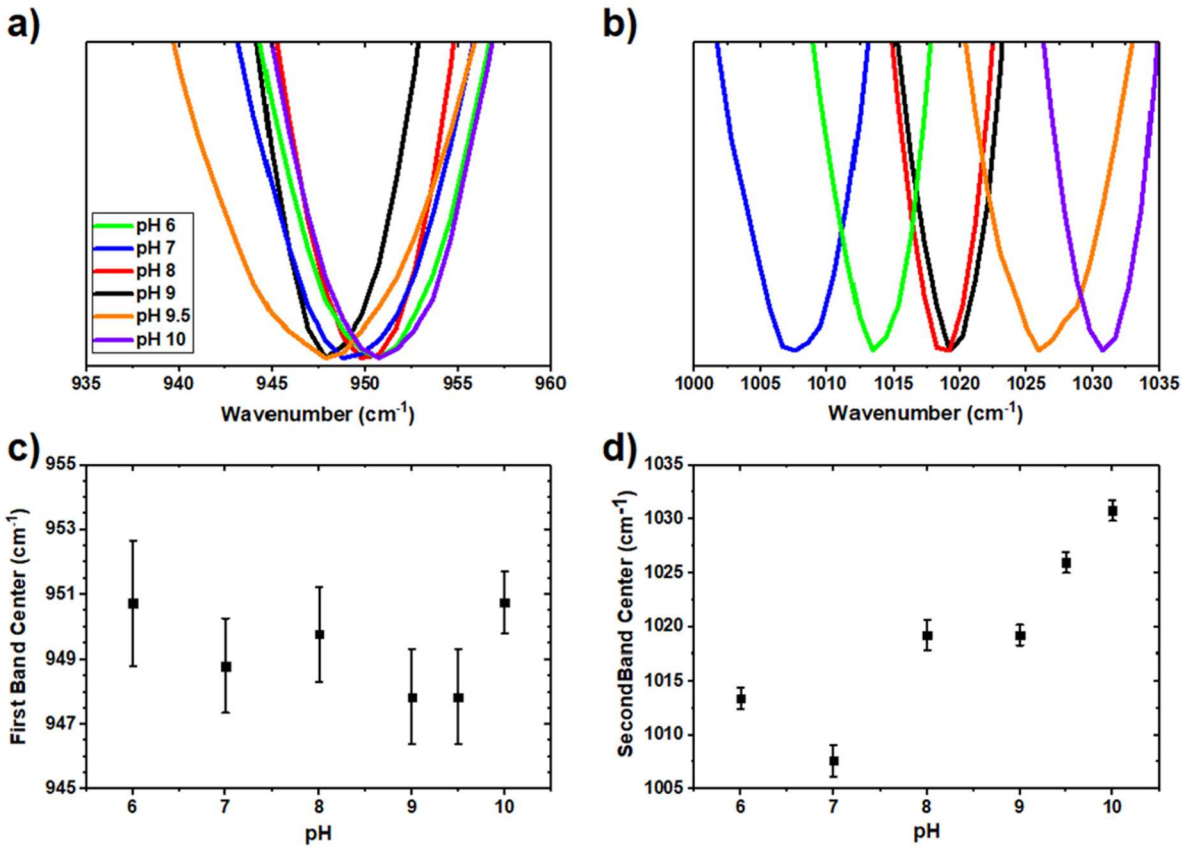

Figure 23: (a, b) FTIR spectra showing (a) Ga–O and (b) Ga–OH bending modes for hydrothermally grown GaOOH microcrystals synthesized at varying pH values. (c, d) Corresponding peak center frequencies of (c) Ga–O and (d) Ga–OH bending modes plotted as a function of synthesis pH. Error bars represent the uncertainty from the best-fit Voigt profiles.

Results for β-Ga_2O_3

The GaOOH precursor particles characterized and discussed above, were subjected to calcination in a furnace to form β-Ga_2O_3. Initial characterization focused on morphological comparison of the specimens before and after calcination, as shown in Figure 24, where it was observed that the particle shape and morphology remain largely unchanged. XRDS analysis of the calcinated GaOOH (Figure 25) reveals diffraction peaks consistent with a monoclinic β-Ga_2O_3 phase, matching literature reports [87, 88] and exhibiting no evidence of secondary phases due to the presence of other polymorphs of Ga_2O_3.

Temperature-dependent Raman spectroscopy measurements (Figures 26 and 27) were performed to probe the vibrational properties and thermal stability of the microcrystals. The observed Raman peak frequencies align well with values reported in the literature (e.g., Ref. 89).

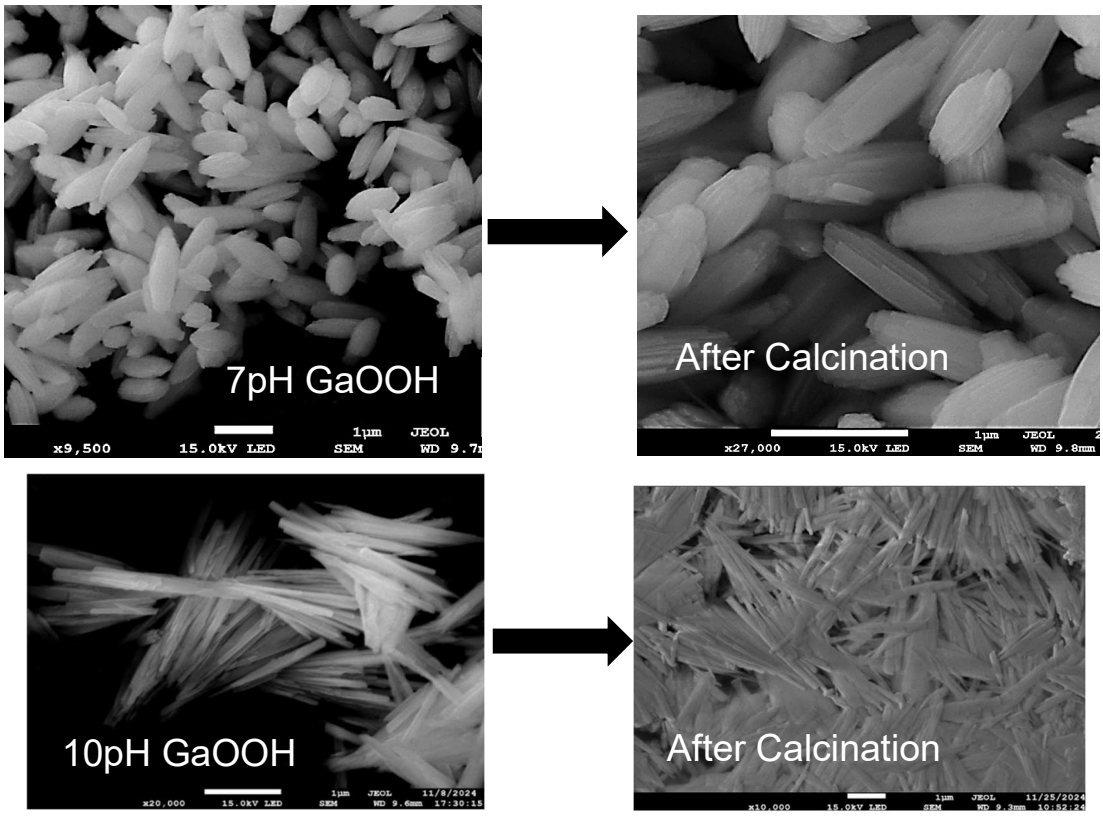

Figure 24: SEM images of GaOOH particles before and after calcination. There is no significant change in morphology after calcination at ~900 ℃ for 5 hours.

The persistence of well-defined phononic modes up to 580 K demonstrates the high crystallinity and thermal stability of the synthesized β-Ga_2O_3. This structural integrity is further corroborated by XRDS data (Figure 25), which display intense and narrow diffraction peaks indicative of a highly ordered lattice. These results confirm the successful synthesis and excellent crystalline quality of the synthesized β-Ga_2O_3 microparticles. Studies of defect-related are needed to elucidate their optoelectronic behavior. Due to the exceptionally wide bandgap of β-Ga_2O_3, future optical characterization will require instrumentation capable of accessing higher-energy (deep-UV) spectral regions to investigate potential variations between near-band-edge and defect-mediated emission mechanisms.

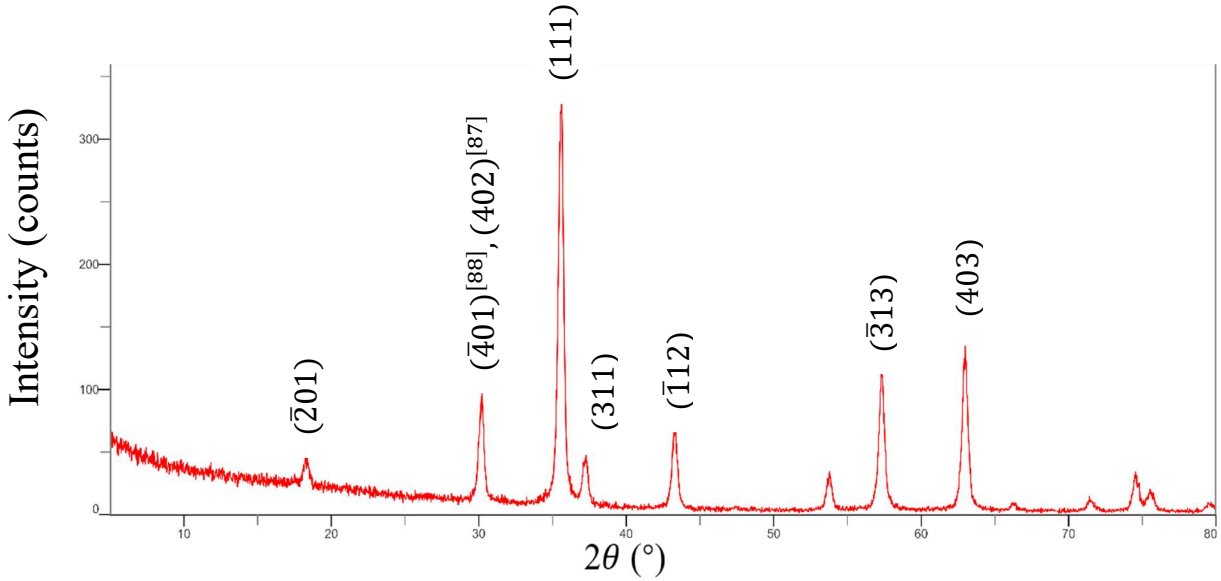

Figure 25: XRD pattern of the calcined sample synthesized at an initial pH of 8. Using Refs. 87 and 88 to assign Miller indices to the constructive diffraction peaks, we observe that most of the major reflections correspond to the β-Ga_2O_3 phase—specifically the (402), (111), and (311) crystallographic planes. The (202) plane, however, is not clearly distinguishable. This absence may be attributed to the proximity of the (202) and (111) peaks, combined with the limited resolution of the wide-angle scan (at approximately 30.4° and 31.7°, respectively).

At the proof-of-concept stage of our studies of hydrogenation effects, we used commercially available (MSE Supplies) micro-crystalline β-Ga_2O_3 powders. A 30 minute remote hydrogen plasma treatment of the samples was performed in a high-vacuum environment.

Optical absorption spectroscopy was run on the samples to investigate changes in optical processes due to hydrogenation. Figure 28 shows the UV/Vis region of the spectra, indicating altered electronic structure due to hydrogenation, which also explains the sample's subtle red/orange tint. The point of the greatest increase of absorption occurs at ~ 4.71 eV, the bandgap energy, which does not change after hydrogenation, as seen in Figure 29.

Time-resolved radioluminescence (RL) spectroscopy (400–800 nm) and thermoluminescence spectroscopy (25–300 °C) measurements were performed to investigate changes in defect-related properties induced by hydrogenation. Figure 30 compares the emission intensity across photon energies associated with recombination centers in β-Ga_2O_3 before and after hydrogenation. The RL spectra reveal that hydrogenation does not modify the inherent recombination mechanisms, with emission energies ranging from 1.46 eV to 3.10 eV corresponding to mid-gap recombination centers. Figure 31 shows that hydrogenation markedly decreases the thermoluminescence intensity while preserving the peak positions. These results strongly support the interpretation that hydrogen primarily passivates existing traps rather than generating new defect states.

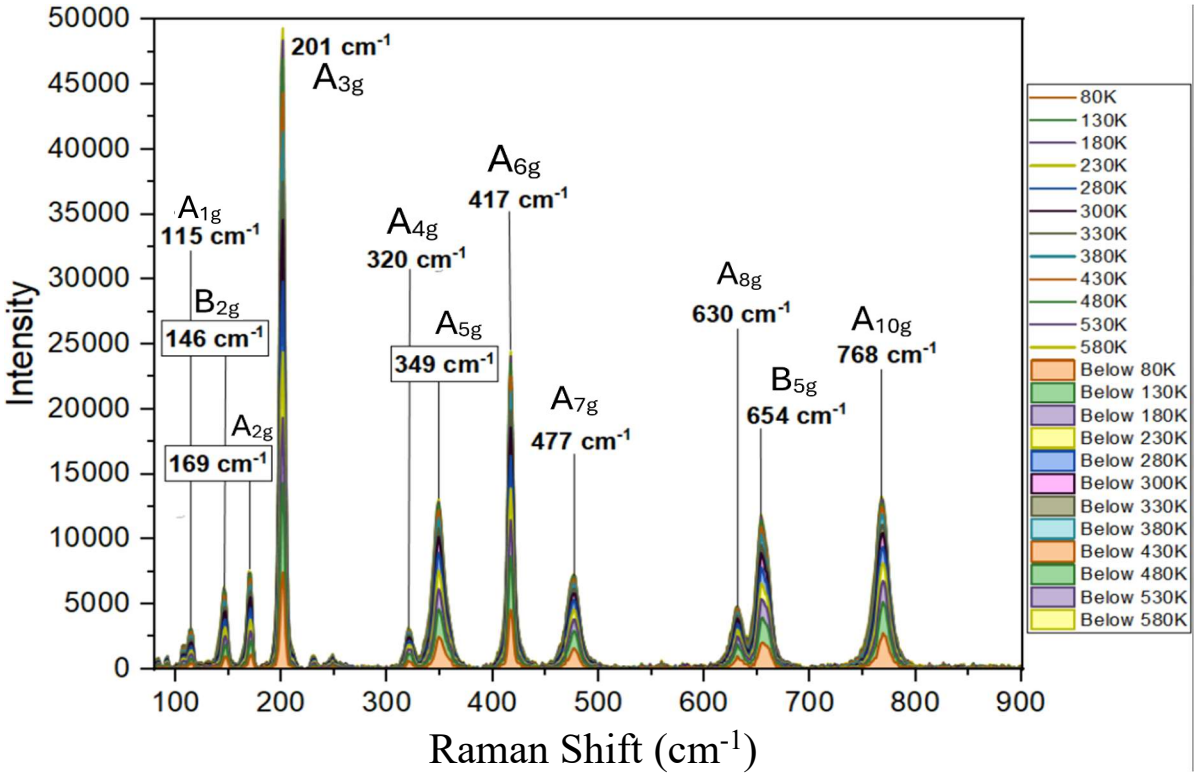

Figure 26: T-Raman spectra of the β-Ga_2O_3 (5 pH) sample collected over a temperature range of 80 K to 580 K, with the corresponding vibrational frequencies assigned to their respective symmetries (Ref. 89).

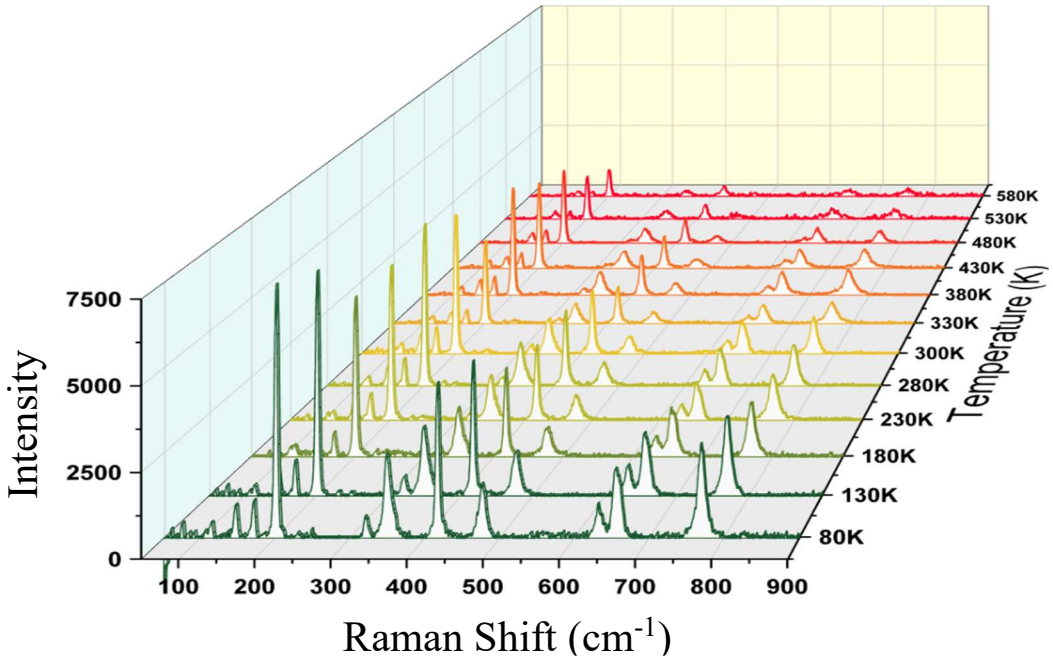

Figure 27: Temperature-dependent Raman spectra demonstrate the thermal stability of the β-Ga_2O_3 (5 pH) microcrystals, showing a decrease in peak intensity with increasing temperature. Despite the expected reduction in signal magnitude, the phononic modes corresponding to each vibrational symmetry remain identifiable and stable up to 580 K, indicating the structural resilience and high quality of the material under elevated thermal conditions.

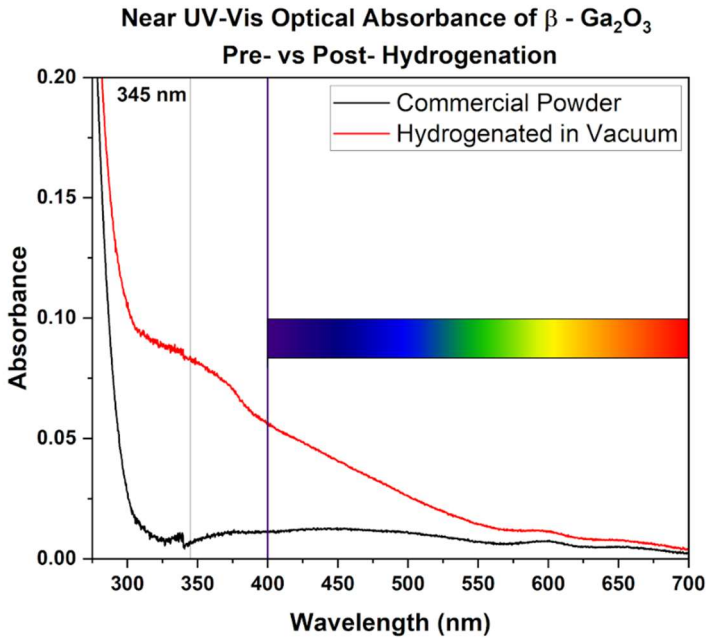

Figure 28: Juxtaposed absorption spectra of the as-received MSE supplies commercial microcrystalline β-Ga_2O_3 sample and the remote hydrogen plasma treated one. The visible spectrum is overlaid as a rectangular rainbow gradient to provide energy context across the measured range. The hydrogenated sample exhibits enhanced absorption in both the UV and visible regions.

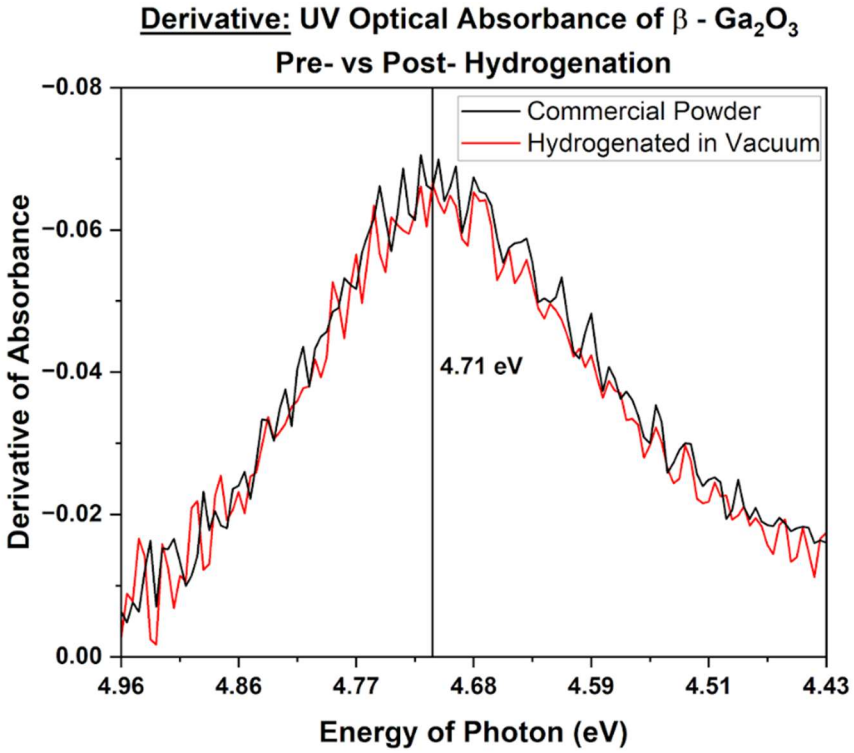

Figure 29: First derivative of the optical absorption spectra in the deep-UV region for the as-received commercial microcrystalline β-Ga_2O_3 sample and the remote hydrogen plasma treated one. The vertical line denotes the approximate energy of near-band-edge (NBE) transition. This comparison shows that hydrogenation does not significantly alter the NBE absorption.

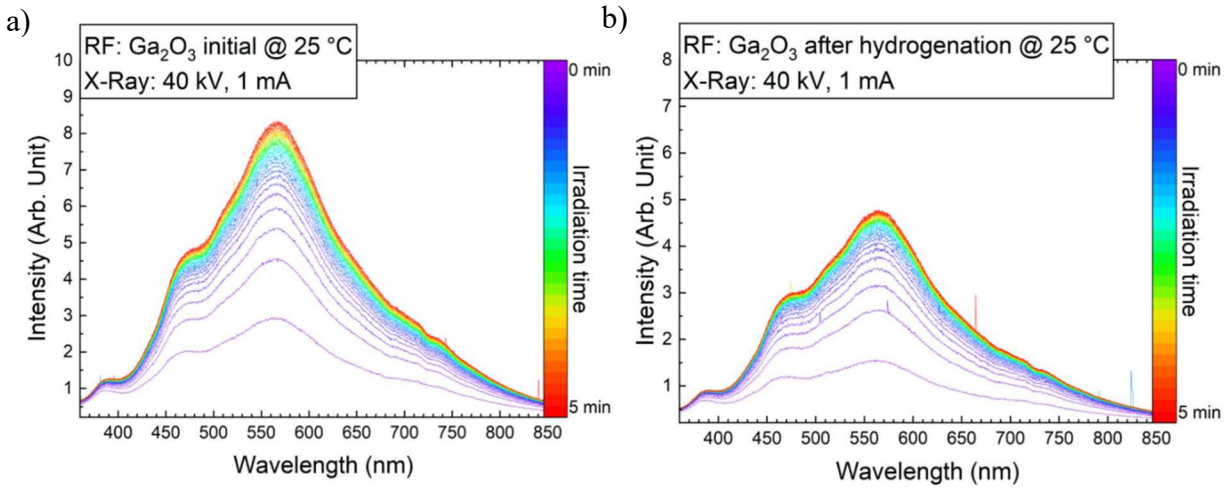

Figure 30: Time-resolved radioluminescence spectra under X-ray excitation measured from 0 to 5 minutes at 25 °C for (a) as-received and (b) hydrogenated β-Ga_2O_3 samples. Following hydrogenation, overall luminescence intensity is reduced while the spectral shape and peak position remain unchanged, indicating defect passivation without alteration of intrinsic luminescent.

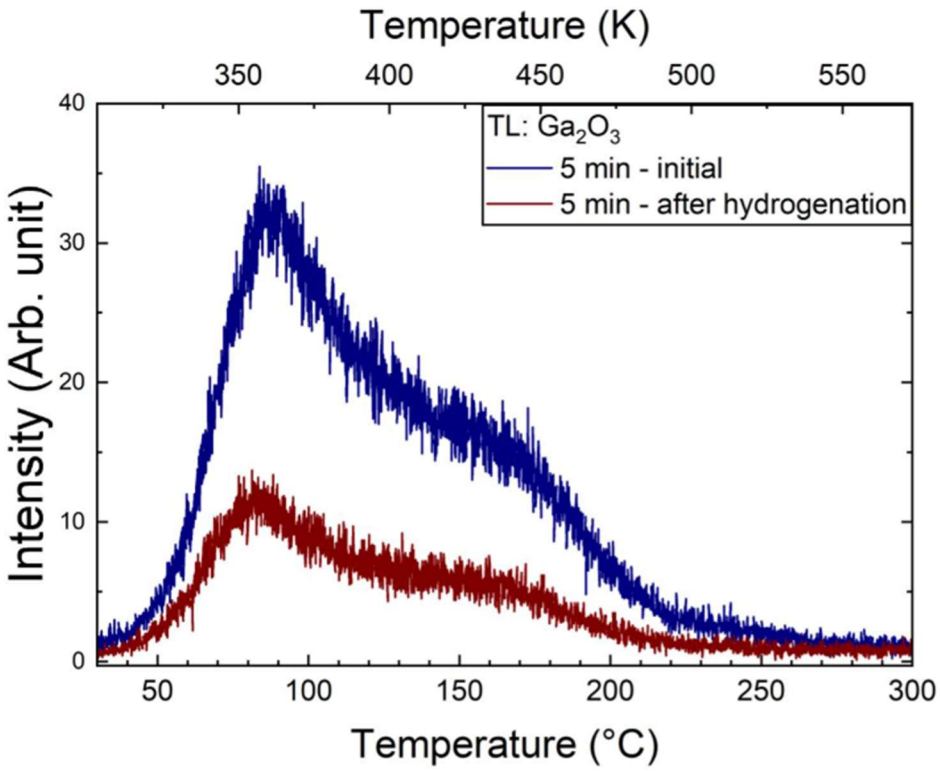

Figure 31: TL spectra of β-Ga_2O_3 recorded after 5 minutes of X-ray irradiation for commercial (blue) and hydrogenated (red) samples. Following hydrogenation, overall TL intensity decreases markedly while the peak position remains constant, indicating effective passivation of native traps without introducing new defect states or altering trap depth energetics.

CONCLUSIONS

In our ZnO microparticles, high-quality crystalline structures appear with mixed surface abundances and morphology. Average sizes for the undoped ZnO particles were measured to be on the order of a micron. However, contrary to literature, it was observed for the Fe-doped particles that the size either increases or remains largely the same.

For systematic studies of ZnO bacterial inhibition via surface interactions, better control over polar and non-polar surface abundances is necessary because Fe contributions depend on the existing defect concentrations and defect types on polar and non-polar surfaces. Our doping procedure is reliable and predictable.

A bandgap redshift was observed at an increasing amount of Fe incorporated into the ZnO lattice, along with a lower intensity of luminescence without changes in relative defect/NBE intensities. Rather, an overall reduction of luminescence intensity was observed. Increase in the disorder in the ZnO lattice could be attributed to the Fe doping, which would increase non-radiative pathways.

In antibacterial testing of the synthesized ZnO crystals, the majority of undoped particles have shown little to no inhibition to log phase *S. Aureus* bacteria, contrary to a majority of the literature, and this warrants further investigation. Bacterial inhibition has been observed in some samples, thus further analysis and characterization of the particles are necessary to identify plausible reasons for these inconsistencies.

High-crystallinity microscale GaOOH has been obtained. Morphology of microcrystals was controlled via pH of the reaction environment (between 6pH and 10pH). Specifically, the long-axis dimensions consistently increased with the pH levels.

GaOOH particles demonstrated a substantial inhibition of the Gram-positive bacteria *S. aureus* and moderate inhibition of the Gram-negative bacteria *E. coli*. We attribute this

discrepancy to the difference between the bacterial envelopes, as Gram-negative bacteria have two membranes separated by a peptidoglycan wall rather than a thicker peptidoglycan wall surrounding one membrane, as seen in Gram-positive bacteria.

A relationship was established between the concentration of optically-active defects, the pH of the reaction precursors, morphology of the microparticles, and their ability to inhibit bacteria. Also, a blueshift in FTIR-ATR spectra with pH of synthesis solution was observed for the Ga-OH vibrational mode. This is important because the Ga-OH bending modes are susceptible to surface-specific changes such as increased incorporation and deprotonation of hydroxyl groups, and/or formation of defect sites that introduce local strain and distortion around these groups. It would be important to study surface defects present in the GaOOH microcrystals via SPV and PLS.

We demonstrated a procedure resulting in high-quality thermally resistant crystalline structures of β-Ga_2O_3 to be used for studies of antibacterial action.

Using commercial microscale powders of β-Ga_2O_3, we observed that remote hydrogen plasma altered electronic transitions and optically-active defect states related to middle-bandgap energies. These results show a quenching of deep-bandgap defect states without alteration of luminescent centers present in the material. The effect of remote hydrogen plasma did not affect the energy of the bandgap in β-Ga_2O_3. To use PLS on these microparticles, a deeper UV source is needed to generate NBE excitonic activity. Specifically, cryogenic PLS studies (~ 10 K) would be necessary for identification of shallow donor behavior due to hydrogenation of β-Ga_2O_3.

REFERENCES

1. Alhalili, Z. Metal Oxides Nanoparticles: General Structural Description, Chemical, Physical, and Biological Synthesis Methods, Role in Pesticides and Heavy Metal Removal through Wastewater Treatment. *Molecules* **2023**, *28* (7), 3086. https://doi.org/10.3390/molecules28073086.

2. Mujahid, M. H.; Upadhyay, T. K.; Khan, F.; Pandey, P.; Park, M. N.; Sharangi, A. B.; Saeed, M.; Upadhye, V. J.; Kim, B. Metallic and Metal Oxide-Derived Nanohybrid as a Tool for Biomedical Applications. *Biomedicine & Pharmacotherapy* **2022**, *155*, 113791. https://doi.org/10.1016/j.biopha.2022.113791.

3. Khalil, M.; Jan, B. M.; Tong, C. W.; Berawi, M. A. Advanced Nanomaterials in Oil and Gas Industry: Design, Application and Challenges. *Applied Energy* **2017**, *191*, 287–310. https://doi.org/10.1016/j.apenergy.2017.01.074.

4. Rao, C. N. R.; Subba Rao, G. V. *Transition Metal Oxides*; An Introduction to Their Electronic Structure and Properties; Springer: Berlin, 2013.

5. Nowotny, J. *Oxide Semiconductors for Solar Energy Conversion: Titanium Dioxide*; CRC Press: Boca Raton, 2016.

6. Mohammed, Aeshah M., Mohammed Mohammed, Jawad K. Oleiwi, et al. "Comprehensive Review on Zinc Oxide Nanoparticle Production and the Associated Antibacterial Mechanisms and Therapeutic Potential." *Nano Trends* 11 (September 2025): 100145. https://doi.org/10.1016/j.nwnano.2025.100145.

7. Vyas, S. A Short Review on Properties and Applications of Zinc Oxide Based Thin Films and Devices: ZnO as a Promising Material for Applications in Electronics, Optoelectronics, Biomedical and Sensors. *Johnson Matthey Technology Review* **2020**, *64* (2), 202–218. https://doi.org/10.1595/205651320X15694993568524.

8. Nabil, M.; Perez-Quintana, I. V.; Acosta, M.; Mendez-Gamboa, J. A.; Castro-Rodriguez, R. Morphological, Structural, and Optical Bandgap Characterization of Extracted ZnO Nanoparticles from Commercial Paste. *Advances in Materials Science and Engineering* **2021**, *2021* (1), 9926544. https://doi.org/10.1155/2021/9926544.

9. Holt, D. B.; Yacobi, B. G. *Extended Defects in Semiconductors*; Cambridge University Press: New York, 2007.

10. Borah, D.; Baruah, M. K.; Saikia, P. P.; Senapoty, K. K.; Barua, M.; Singha, R. Structural Characterization and Surface Environment of ZnO Nanoflowers. **2016**.

11. Mora-Fonz, D.; Buckeridge, J.; Logsdail, A. J.; Scanlon, D. O.; Sokol, A. A.; Woodley, S.; Catlow, C. R. A. Morphological Features and Band Bending at Nonpolar Surfaces of

ZnO. *J. Phys. Chem. C* **2015**, *119* (21), 11598–11611. https://doi.org/10.1021/acs.jpcc.5b01331.

12. ResearchGate. “Figure 1: ZnO Unit Cell with Wurtzite Structure. b Various Crystal...” Accessed October 28, 2025. https://www.researchgate.net/figure/ZnO-unit-cell-with-wurtzite-structure-b-Various-crystal-planes-of-ZnO-Wurtzite-structure_fig5_269577964.

13. Schmidt-Mende, L.; MacManus-Driscoll, J. L. ZnO – Nanostructures, Defects, and Devices. *Materials Today* **2007**, *10* (5), 40–48. https://doi.org/10.1016/S1369-7021(07)70078-0.

14. Johnson, D.; Reeks, J. M.; Caron, A.; Tzoka, I.; Ali, I.; McGillivray, S. M.; Strzhemechny, Y. M. Influence of Surface Properties and Microbial Growth Media on Antibacterial Action of ZnO. *Coatings* **2022**, *12* (11), 1648. https://doi.org/10.3390/coatings12111648.

15. Mora-Fonz, D.; Lazauskas, T.; Farrow, M. R.; Catlow, C. R. A.; Woodley, S. M.; Sokol, A. A. Why Are Polar Surfaces of ZnO Stable? *Chem. Mater.* **2017**, *29* (12), 5306–5320. https://doi.org/10.1021/acs.chemmater.7b01487.

16. Xie, Yanping, Yiping He, Peter L. Irwin, Tony Jin, and Xianming Shi. “Antibacterial Activity and Mechanism of Action of Zinc Oxide Nanoparticles against Campylobacter Jejuni.” *Applied and Environmental Microbiology* 77, no. 7 (2011): 2325–31. https://doi.org/10.1128/AEM.02149-10.

17. Reeks, J. Interactions of Nano- and Microcrystalline ZnO with Staphylococcus Aureus and Bacterial Growth Media: Optoelectronic Probes, Microscopy and Biological Assays. Ph.D., Texas Christian University, United States -- Texas, 2021. https://www.proquest.com/docview/2609414058/abstract/779B1D4B665F4F23PQ/1 (accessed 2025-10-17).

18. Johnson, D. Role of Interfacial Phenomena in Antibacterial Applications of Metal Oxide Semiconductors. Ph.D., Texas Christian University, United States -- Texas, 2025. https://www.proquest.com/docview/3201273608/abstract/C374C9AD17C4365PQ/1 (accessed 2025-10-17).

19. Caron, A. J.; Ali, I. J.; Delgado, M. J.; Johnson, D.; Reeks, J. M.; Strzhemechny, Y. M.; McGillivray, S. M. Zinc Oxide Nanoparticles Mediate Bacterial Toxicity in Mueller-Hinton Broth via Zn2+. *Front. Microbiol.* **2024**, *15*. https://doi.org/10.3389/fmicb.2024.1394078.

20. Jiang, Shengjie, Kaili Lin, and Ming Cai. “ZnO Nanomaterials: Current Advancements in Antibacterial Mechanisms and Applications.” *Frontiers in Chemistry* 8 (July 2020). https://doi.org/10.3389/fchem.2020.00580.

21. Jin, Su-Eon, and Hyo-Eon Jin. “Antimicrobial Activity of Zinc Oxide Nano/Microparticles and Their Combinations against Pathogenic Microorganisms for Biomedical Applications: From Physicochemical Characteristics to Pharmacological Aspects.” *Nanomaterials* 11, no. 2 (2021): 263. https://doi.org/10.3390/nano11020263.

22. Mendes, Carolina Rosai, Guilherme Dilarri, Carolina Froes Forsan, et al. “Antibacterial Action and Target Mechanisms of Zinc Oxide Nanoparticles against Bacterial Pathogens.” *Scientific Reports* 12, no. 1 (2022): 2658. https://doi.org/10.1038/s41598-022-06657-y.

23. Zhang, Lingling, Yunhong Jiang, Yulong Ding, Malcolm Povey, and David York. “Investigation into the Antibacterial Behaviour of Suspensions of ZnO Nanoparticles (ZnO Nanofluids).” *Journal of Nanoparticle Research* 9, no. 3 (2007): 479–89. https://doi.org/10.1007/s11051-006-9150-1.

24. Baldini, M.; Galazka, Z.; Wagner, G. Recent Progress in the Growth of β-Ga2O3 for Power Electronics Applications. *Materials Science in Semiconductor Processing* **2018**, *78*, 132–146. https://doi.org/10.1016/j.mssp.2017.10.040.

25. (PDF) Preparations, Properties and Applications of Gallium Oxide Nanomaterials – A Review. *ResearchGate*. https://doi.org/10.1002/nano.202100149.

26. Litimein, F.; Rached, D.; Khenata, R.; Baltache, H. FPLAPW Study of the Structural, Electronic, and Optical Properties of Ga2O3: Monoclinic and Hexagonal Phases. *Journal of Alloys and Compounds* **2009**, *488* (1), 148–156. https://doi.org/10.1016/j.jallcom.2009.08.092.

27. ResearchGate. “Distinct Unit Cell Structure of Different Polymorphs of Gallium Oxide....” Accessed October 28, 2025. https://www.researchgate.net/figure/Distinct-Unit-cell-structure-of-different-polymorphs-of-Gallium-Oxide-The-differences-in_fig3_390049026.

28. Chikoidze, E.; Fellous, A.; Perez-Tomas, A.; Sauthier, G.; Tchelidze, T.; Ton-That, C.; Huynh, T. T.; Phillips, M.; Russell, S.; Jennings, M.; Berini, B.; Jomard, F.; Dumont, Y. P-Type β-Gallium Oxide: A New Perspective for Power and Optoelectronic Devices. *Materials Today Physics* **2017**, *3*, 118–126. https://doi.org/10.1016/j.mtphys.2017.10.002.

29. ResearchGate. “Monoclinic Structure of β-Ga2O3. The Color Code of Inequivalent Sites...” Accessed October 28, 2025. https://www.researchgate.net/figure/Monoclinic-structure-of-b-Ga2O3-The-color-code-of-inequivalent-sites-is-shown-The_fig1_378836436.

30. McCluskey, M. D. Point Defects in Ga2O3. *J. Appl. Phys.* **2020**, *127* (10), 101101. https://doi.org/10.1063/1.5142195.

31. Yang, Y.; Shi, Z.; Zang, H.; Ma, X.; Fan, D.; Bai, J.; Zhang, F.; Jiang, K.; Lv, S.; Li, S.; Sun, X.; Li, D. How Do the Oxygen Vacancies Affect the Photoexcited Carriers Dynamics in β-Ga2O3 ? . *Materials Today Physics* **2024**, *40*, 101328. https://doi.org/10.1016/j.mtphys.2024.101328.

32. Wu, G.; Guo, X.; Zhang, F.; Zhong, X.; Wang, J.; Guo, D. Radiation Damage Mechanisms in β-Ga2O3 MSM Solar-Blind Photodetectors: Insights from Proton, Neutron, and γ-Ray Irradiation. *IEEE Electron Device Letters* **2025**, 1–1. https://doi.org/10.1109/LED.2025.3605225.

33. Dittrich, Th.; Parisini, A.; Pavesi, M.; Baraldi, A.; Sacchi, A.; Mezzadri, F.; Mazzolini, P.; Bosi, M.; Seravalli, L.; Bosio, A.; Fornari, R. Electronic States near Surfaces and Interfaces of β-Ga2O3 and κ-Ga2O3 Epilayers Investigated by Surface Photovoltage Spectroscopy, Photoconductivity and Optical Absorption. *Surfaces and Interfaces* **2024**, *51*, 104642. https://doi.org/10.1016/j.surfin.2024.104642.

34. Wang, Y.; Li, S.; Cao, J.; Jiang, Y.; Zhang, Y.; Tang, W.; Wu, Z. Improved Response Speed of β-Ga2O3 Solar-Blind Photodetectors by Optimizing Illumination and Bias. *Materials & Design* **2022**, *221*, 110917. https://doi.org/10.1016/j.matdes.2022.110917.

35. Wang, Yimei, Xuechao Shi, Shuxian Hou, et al. "Gallium Oxide Nanoparticles With Controllable Morphologies as Effective Photocatalytic Antimicrobial Agents." *Applied Organometallic Chemistry* 39, no. 8 (2025): e70305. https://doi.org/10.1002/aoc.70305.

36. Kang, X.-Q.; Shu, G.-F.; Jiang, S.-P.; Xu, X.-L.; Qi, J.; Jin, F.-Y.; Liu, D.; Xiao, Y.-H.; Lu, X.-Y.; Du, Y.-Z. Effective Targeted Therapy for Drug-Resistant Infection by ICAM-1 Antibody-Conjugated TPGS Modified β-Ga_2O_3:Cr^{3+} Nanoparticles. *Theranostics* **2019**, *9* (10), 2739–2753. https://doi.org/10.7150/thno.33452.

37. Choi, S.; Hassan, M. A.; Britigan, B. E.; Narayanasamy, P. Antimicrobial Activity of Gallium(III) Compounds: Pathogen-Dependent Targeting of Multiple Iron/Heme-Dependent Biological Processes. *Current Issues in Molecular Biology* **2024**, *46* (8), 9149–9161. https://doi.org/10.3390/cimb46080541.

38. Li, F.; Liu, F.; Huang, K.; Yang, S. Advancement of Gallium and Gallium-Based Compounds as Antimicrobial Agents. *Front. Bioeng. Biotechnol.* **2022**, *10*. https://doi.org/10.3389/fbioe.2022.827960.

39. “Antibacterial Activity and Mechanistic Insights of Gallium-Based Nanoparticles: An Emerging Frontier in Metal-Based Antimicrobials.” *RSC Advances* 15, no. 38 (2025): 31122–53. https://doi.org/10.1039/d5ra04216j.

40. Radha, Remya, Ahmad Fawad, Sreeshna Ravindran, Ganjaboy Boltaev, Sachin Philip, and Mohammad H. Al-Sayah. “Enhanced Antimicrobial and Biofilm-Disrupting Properties of Gallium-Doped Carbon Dots.” *ACS Omega* 10, no. 25 (2025): 27559–74. https://doi.org/10.1021/acsomega.5c03575.

41. Shi, Fengjun, SiSi Ma, Sen Liu, et al. “A Novel Antimicrobial Strategy for Bacterial Infections: Gallium-Based Materials.” *Colloid and Interface Science Communications* 56 (September 2023): 100735. https://doi.org/10.1016/j.colcom.2023.100735.

42. Islam, M. M.; Liedke, M. O.; Winarski, D.; Butterling, M.; Wagner, A.; Hosemann, P.; Wang, Y.; Uberuaga, B.; Selim, F. A. Chemical Manipulation of Hydrogen Induced High P-Type and n-Type Conductivity in Ga2O3. *Sci Rep* **2020**, *10* (1), 6134. https://doi.org/10.1038/s41598-020-62948-2.

43. Jiang, Shengjie, Kaili Lin, and Ming Cai. “ZnO Nanomaterials: Current Advancements in Antibacterial Mechanisms and Applications.” *Frontiers in Chemistry* 8 (July 2020). https://doi.org/10.3389/fchem.2020.00580.

44. Mohammed, Aeshah M., Mohammed Mohammed, Jawad K. Oleiwi, et al. “Comprehensive Review on Zinc Oxide Nanoparticle Production and the Associated Antibacterial Mechanisms and Therapeutic Potential.” *Nano Trends* 11 (September 2025): 100145. https://doi.org/10.1016/j.nwnano.2025.100145.

45. Babayevska, Nataliya, Łucja Przysiecka, Igor Iatsunskyi, et al. “ZnO Size and Shape Effect on Antibacterial Activity and Cytotoxicity Profile.” *Scientific Reports* 12, no. 1 (2022): 8148. https://doi.org/10.1038/s41598-022-12134-3.

46. Mendes, Ana Rita, Carlos M. Granadeiro, Andreia Leite, Eulália Pereira, Paula Teixeira, and Fátima Poças. “Optimizing Antimicrobial Efficacy: Investigating the Impact of Zinc Oxide Nanoparticle Shape and Size.” *Nanomaterials* 14, no. 7 (2024): 638. https://doi.org/10.3390/nano14070638.

47. Hwang, Changha, Min-Ha Choi, Hyoun-Ee Kim, Seol-Ha Jeong, and Ji-Ung Park. “Reactive Oxygen Species-Generating Hydrogel Platform for Enhanced Antibacterial Therapy.” *NPG Asia Materials* 14, no. 1 (2022): 72. https://doi.org/10.1038/s41427-022-00420-5.

48. Johnson, D. A.; Reeks, J. M.; Caron, A. J.; McGillivray, S. M.; Wiglusz, R. J.; Strzhemechny, Y. M. Surface Photovoltage Response of ZnO to Phosphate-Buffered Saline Solution with and without Presence of Staphylococcus Aureus. *Nanomaterials (Basel)* **2023**, *13* (10), 1652. https://doi.org/10.3390/nano13101652.

49. Foster, T. Staphylococcus. In *Medical Microbiology*; Baron, S., Ed.; University of Texas Medical Branch at Galveston: Galveston (TX), 1996.

50. Reeks, J. M.; Ali, I.; Moss, W. J.; Davis, E.; McGillivray, S. M.; Strzhemechny, Y. M. Microscale ZnO with Controllable Crystal Morphology as a Platform to Study Antibacterial Action on Staphylococcus Aureus. *Biointerphases* **2021**, *16* (3), 031003. https://doi.org/10.1116/6.0000957.\

51. Silva, B. L. da; Abuçafy, M. P.; Manaia, E. B.; Junior, J. A. O.; Chiari-Andréo, B. G.; Pietro, R. C. R.; Chiavacci, L. A. <p>Relationship Between Structure And Antimicrobial Activity Of Zinc Oxide Nanoparticles: An Overview</P>. *IJN* **2019**, *14*, 9395–9410. https://doi.org/10.2147/IJN.S216204.

52. Li, Y.; Liao, C.; Tjong, S. C. Recent Advances in Zinc Oxide Nanostructures with Antimicrobial Activities. *International Journal of Molecular Sciences* **2020**, *21* (22), 8836. https://doi.org/10.3390/ijms21228836.

53. Xie, Yanping, Yiping He, Peter L. Irwin, Tony Jin, and Xianming Shi. "Antibacterial Activity and Mechanism of Action of Zinc Oxide Nanoparticles against Campylobacter Jejuni." *Applied and Environmental Microbiology* 77, no. 7 (2011): 2325–31. https://doi.org/10.1128/AEM.02149-10.

54. Xiao, J. Stabilization Mechanism of ZnO Nanoparticles by Fe Doping. *Phys. Rev. Lett.* **2014**, *112* (10). https://doi.org/10.1103/PhysRevLett.112.106102.

55. Kurtuldu, Fatih, Nurshen Mutlu, Aldo R. Boccaccini, and Dušan Galusek. "Gallium Containing Bioactive Materials: A Review of Anticancer, Antibacterial, and Osteogenic Properties." *Bioactive Materials* 17 (November 2022): 125–46. https://doi.org/10.1016/j.bioactmat.2021.12.034.

56. Qu, Chun-Chun, Yu-Tong Liang, Xi-Qing Wang, Shang Gao, Zhi-Zhu He, and Xu-Yang Sun. "Gallium-Based Liquid Metal Materials for Antimicrobial Applications." *Bioengineering* 9, no. 9 (2022): 416. https://doi.org/10.3390/bioengineering9090416.

57. Murphy, Bríd, Carolina Martins, Mimma Maggio, Mick A. Morris, and David A. Hoey. "Nano Sized Gallium Oxide Surface Features for Enhanced Antimicrobial and Osteo-

Integrative Responses." *Colloids and Surfaces B: Biointerfaces* 227 (July 2023): 113378. https://doi.org/10.1016/j.colsurfb.2023.113378.

58. Xie, Tingting, Yuchen Qi, Yangyang Li, et al. "Ultrasmall Ga-ICG Nanoparticles Based Gallium Ion/Photodynamic Synergistic Therapy to Eradicate Biofilms and against Drug-Resistant Bacterial Liver Abscess." *Bioactive Materials* 6, no. 11 (2021): 3812–23. https://doi.org/10.1016/j.bioactmat.2021.03.032.

59. Qiao, Yue, Yangyang Li, Yang Ye, et al. "Gallium-Based Nanoplatform for Combating Multidrug-Resistant Pseudomonas Aeruginosa and Postoperative Inflammation in Endophthalmitis Secondary to Cataract Surgery." *ACS Applied Materials & Interfaces* 14, no. 46 (2022): 51763–75. https://doi.org/10.1021/acsami.2c15834.

60. Johnson, D. A., P. Ahluwalia, J. H. Brannon, et al. "Influence of Morphology and Surface Properties on the Antibacterial Action of GaOOH Microparticles." *Biointerphases* 20, no. 1 (2025): 011004. https://doi.org/10.1116/6.0004133.

61. Zhang, J.; Liu, Z.; Lin, C.; Lin, J. A Simple Method to Synthesize β-Ga2O3 Nanorods and Their Photoluminescence Properties. *Journal of Crystal Growth* **2005**, *280* (1), 99–106. https://doi.org/10.1016/j.jcrysgro.2005.02.060.

62. "A Simple Synthesis of Ga2O3 and GaN Nanocrystals." n.d. Accessed October 19, 2025. https://pubs.rsc.org/en/content/articlepdf/2017/ra/c7ra10639d.

63. Girija, K., S. Thirumalairajan, and D. Mangalaraj. "Morphology Controllable Synthesis of Parallely Arranged Single-Crystalline β-Ga2O3 Nanorods for Photocatalytic and Antimicrobial Activities." *Chemical Engineering Journal* 236 (January 2014): 181–90. https://doi.org/10.1016/j.cej.2013.09.088.

64. Reinertsen, Vilde M., Philip M. Weiser, Ymir K. Frodason, Marianne E. Bathen, Lasse Vines, and Klaus Magnus Johansen. "Anisotropic and Trap-Limited Diffusion of Hydrogen/Deuterium in Monoclinic Gallium Oxide Single Crystals." *Applied Physics Letters* 117, no. 23 (2020): 232106. https://doi.org/10.1063/5.0027333.

65. Islam, Md Minhazul. "Study of Defects and Doping in β-Ga2O3." Ph.D., Bowling Green State University, 2021. https://www.proquest.com/docview/2595648859/abstract/D97B7CB8AF424628PQ/1.

66. Zhang, Z., E. Farzana, A. R. Arehart, and S. A. Ringel. "Deep Level Defects throughout the Bandgap of (010) β-Ga2O3 Detected by Optically and Thermally Stimulated Defect

Spectroscopy." *Applied Physics Letters* 108, no. 5 (2016): 052105. https://doi.org/10.1063/1.4941429.

67. Zhu, Xin, Ying-Wu Zhang, Sheng-Nan Zhang, Xiao-Qing Huo, Xing-Hua Zhang, and Zhi-Qing Li. "Defect Energy Levels in Monoclinic β-Ga2O3." *Journal of Luminescence* 246 (June 2022): 118801. https://doi.org/10.1016/j.jlumin.2022.118801.

68. (PDF) Electrical Characterization of Semiconductor Oxide-Based Gas Sensors Using Impedance Spectroscopy: A Review: *ResearchGate* **2025**. https://doi.org/10.1166/rase.2016.1109.

69. da Silva, G. M. G.; Faia, P. M.; Mendes, S. R.; Araújo, E. S. A Review of Impedance Spectroscopy Technique: Applications, Modelling, and Case Study of Relative Humidity Sensors Development. *Applied Sciences* **2024**, *14* (13), 5754. https://doi.org/10.3390/app14135754.

70. Varley, J. B., J. R. Weber, A. Janotti, and C. G. Van De Walle. "Oxygen Vacancies and Donor Impurities in β-Ga2O3." *Applied Physics Letters* 97, no. 14 (2010): 142106. https://doi.org/10.1063/1.3499306.

71. Van de Walle, C. G. Hydrogen as a Cause of Doping in Zinc Oxide. *Phys. Rev. Lett.* **2000**, *85* (5), 1012–1015. https://doi.org/10.1103/PhysRevLett.85.1012.

72. Strzhemechny, Y. M.; Nemergut, J.; Smith, P. E.; Bae, J.; Look, D. C.; Brillson, L. J. Remote Hydrogen Plasma Processing of ZnO Single Crystal Surfaces. *J. Appl. Phys.* **2003**, *94* (7), 4256–4262. https://doi.org/10.1063/1.1606859.

73. Polyakov, A. Y., In-Hwan Lee, N. B. Smirnov, et al. "Hydrogen Plasma Treatment of ***β*** -Ga2O3: Changes in Electrical Properties and Deep Trap Spectra." *Applied Physics Letters* 115, no. 3 (2019): 032101. https://doi.org/10.1063/1.5108790.

74. Varley, J B, H Peelaers, A Janotti, and C G Van De Walle. "Hydrogenated Cation Vacancies in Semiconducting Oxides." *Journal of Physics: Condensed Matter* 23, no. 33 (2011): 334212. https://doi.org/10.1088/0953-8984/23/33/334212.

75. Lallo da Silva, Bruna, Bruno Leonardo Caetano, Bruna Galdorfini Chiari-Andréo, Rosemeire Cristina Linhari Rodrigues Pietro, and Leila Aparecida Chiavacci. "Increased Antibacterial Activity of ZnO Nanoparticles: Influence of Size and Surface Modification." *Colloids and Surfaces B: Biointerfaces* 177 (May 2019): 440–47. https://doi.org/10.1016/j.colsurfb.2019.02.013.

76. *AXIS Supra+ | XPS Surface Analysis | Kratos Analytical*. n.d. Accessed October 22, 2025. https://www.kratos.com/product/axis-supra-xps-surface-analysis-instrument/.

77. *Scanning Electron Microscopy | Nanoscience Instruments*. n.d. Accessed October 28, 2025. https://www.nanoscience.com/techniques/scanning-electron-microscopy/.

78. Universallab. "The Basic Principles and Applications of XRD." Universal Lab Blog, April 15, 2024. https://universallab.org/blog/the_basic_principles_and_applications_of_xrd.

79. Moulder, John F., and Jill Chastain, eds. *Handbook of X-Ray Photoelectron Spectroscopy: A Reference Book of Standard Spectra for Identification and Interpretation of XPS Data*. Update. Perkin-Elmer Corporation, 1992.

80. Cuscó, Ramon, Esther Alarcón-Lladó, Jordi Ibáñez, et al. "Temperature Dependence of Raman Scattering in ZnO." *Physical Review B* 75, no. 16 (2007): 165202. https://doi.org/10.1103/PhysRevB.75.165202.

81. Pilliadugula, Rekha, and N. Gopala Krishnan. "Effect of pH Dependent Morphology on Room Temperature NH3 Sensing Performances of β-Ga2O3." *Materials Science in Semiconductor Processing* 112 (June 2020): 105007. https://doi.org/10.1016/j.mssp.2020.105007.

82. Krehula, Stjepko, Mira Ristić, Shiro Kubuki, Yusuke Iida, Martin Fabián, and Svetozar Musić. "The Formation and Microstructural Properties of Uniform α-GaOOH Particles and Their Calcination Products." *Journal of Alloys and Compounds* 620 (January 2015): 217–27. https://doi.org/10.1016/j.jallcom.2014.09.134.

83. Sun, Wenyue, Manlin Qi, Shi Cheng, Chunyan Li, Biao Dong, and Lin Wang. "Gallium and Gallium Compounds: New Insights into the 'Trojan Horse' Strategy in Medical Applications." *Materials & Design* 227 (March 2023): 111704. https://doi.org/10.1016/j.matdes.2023.111704.

84. Salton, M. R. J. "The Relationship Between the Nature of the Cell Wall and the Gram Stain." *Microbiology* 30, no. 2 (1963): 223–35. https://doi.org/10.1099/00221287-30-2-223.

85. Zhang, Jie, Zhiguo Liu, Cuikun Lin, and Jun Lin. "A Simple Method to Synthesize β-Ga2O3 Nanorods and Their Photoluminescence Properties." *Journal of Crystal Growth* 280, no. 1 (2005): 99–106. https://doi.org/10.1016/j.jcrysgro.2005.02.060.

86. Hong, Sungmin, Choong Kyun Rhee, and Youngku Sohn. “Photoluminescence, Electro- and Thermal Catalytic Properties of Bare and Eu(III)-Doped GaOOH, α- and β-Ga2O3 Nanorods.” *Journal of Alloys and Compounds* 774 (February 2019): 11–17. https://doi.org/10.1016/j.jallcom.2018.09.381.

87. Luchechko, A., V. Vasyltsiv, M. Kushlyk, et al. “Structural and Luminescence Characterization of β-Ga2O3 Nanopowders Obtained via High-Energy Ball Milling.” *Applied Nanoscience* 13, no. 7 (2023): 5149–55. https://doi.org/10.1007/s13204-022-02717-x.

88. ResearchGate. “XRD Patterns of β-Ga2O3 Products Obtained at Different Hydrothermal Times.” Accessed October 28, 2025. https://www.researchgate.net/figure/XRD-patterns-of-b-Ga2O3-products-obtained-at-different-hydrothermal-times_fig2_344610481.

89. Das, Debabrata, Guillermo Gutierrez, and C. V. Ramana. “Raman Spectroscopic Characterization of Chemical Bonding and Phase Segregation in Tin (Sn)-Incorporated Ga2O3.” *ACS Omega* 8, no. 13 (2023): 11709–16. https://doi.org/10.1021/acsomega.2c05047.

VITA

Personal

John Hunter Brannon

Metairie, Louisiana

March 31st, 2001

Education

Fall 2023 – Present

Texas Christian University

Department of Physics & Astronomy

Graduate Student

Fall 2019 – Spring 2023

Texas Christian University

Department of Physics & Astronomy

Bachelor of Science, Physics

Publications

Johnson, D. A., P. Ahluwalia, **J. H. Brannon**, et al. "Influence of Morphology and Surface Properties on the Antibacterial Action of GaOOH Microparticles." *Biointerphases* 20, no. 1 (2025): 011004. https://doi.org/10.1116/6.0004133.

Oral Presentations

Brannon J. H., et al. "TUNING OF ANTIBACTERIAL ACTION OF ZnO MICROCRYSTALS BY MODIFYING SURFACE DEFECTS WITH Fe-DOPING." NanoBioPhysics: Fundamentals and Applied Aspects 2025, Kharkiv, Ukraine: https://www.ilt.kharkov.ua/nbp2025/program.html

Internships/Workshops

Institute of Low Temperature and Structure Research | July 2025

Kratos Analytical X-ray Photoelectron Spectroscopy Workshop | October 2024

ABSTRACT

OPTOELECTRONIC TRANSPORT AND ANTIBACTERIAL PROPERTIES DRIVEN BY SURFACE DEFECTS IN MICRO- AND NANOSCALE OXIDES OF ZINC AND GALLIUM.

by
John Hunter Brannon

Bachelor of Science, 2023
Texas Christian University
Fort Worth, Texas

Thesis Advisor: Dr. Yuri Strzhemechny

Zinc oxide (ZnO) and beta-gallium oxide (β-Ga_2O_3) are semiconductors with bandgap energies of approximately 3.4 eV and 4.8 eV, respectively. These materials are utilized across diverse applications, including pharmaceuticals, radiation shielding, etc. Our investigation addresses: (1) antimicrobial properties of Zn- and Ga-containing metal oxides, and (2) studies of the role of hydrogen in the persistent n-type conductivity of β-Ga_2O_3. Ga- and Zn-containing metal oxides present alternative antibacterial pathways mediated by surface chemistry and defect states that are not fully understood. β-Ga_2O_3 is promising for high-power electronics, but its persistent n-type behavior restricts applications. Iron doping of ZnO is used to possibly reduce Zn-cation release from surface, a suggested driver of ZnO's antibacterial activity. GaOOH particles with different defect levels and morphologies show varied antibacterial efficacy against S. aureus and E. coli. β-Ga_2O_3 microcrystals are treated with remote hydrogen plasma to elucidate hydrogen's behavior as a contributor to persistent n-type conductivity.